E4BP4 Safeguards Brown Fat Mitochondria from Obesity-Induced Fragmentation via Ceramide Repression

Fernando Valdivieso-Rivera[1,2], Vanessa O. Furino[1], Carlos E. Leher[1], Ariane M. Zanesco[1], Monara Kaélle Cruz[3], Flavia C. Gan[1], Adriana Leandra Santoro[1,4], Lara Regina-Ferreira[1], Giovanna Leite Santos[5], Tiago Tomazini Gonçalves[6], Luiz Osório Leiria[6], Pedro M. Moraes-Vieira[1,3], Roger Frigério Castilho[5], Marcelo A. Mori[1,4,7], Licio A. Velloso[1,5], Carlos H. Sponton[1,8,9*]

[1]Obesity and Comorbidities Research Center, Universidade Estadual de Campinas (UNICAMP), Campinas, Brazil.

[2]Graduate Program in Molecular and Morphofunctional Biology, Universidade Estadual de Campinas (UNICAMP), Campinas, Brazil.

[3]Laboratory of Immunometabolism, Department of Genetics, Evolution, Microbiology and Immunology-Institute of Biology, Universidade Estadual de Campinas (UNICAMP), Campinas, Brazil.

[4]Department of Biochemistry and Tissue Biology, Institute of Biology, Universidade Estadual de Campinas (UNICAMP), Campinas, Brazil.

[5]Department of Pathology, Universidade Estadual de Campinas (UNICAMP), Campinas, Brazil.

[6]Center for Research in Inflammatory Diseases (CRID), Ribeirão Preto Medical School, Universidade de São Paulo (FMRP-USP), Ribeirão Preto, Brazil.

[7]Experimental Medicine Research Cluster, Universidade Estadual de Campinas, Campinas (UNICAMP), Campinas, Brazil

[8]Department of Physiology, Ribeirão Preto Medical School, Universidade de São Paulo (FMRP-USP), Ribeirão Preto, Brazil.

[9]Lead contact

* Correspondence: **csponton@usp.br**

SUMMARY

Brown adipose tissue (BAT) counteracts obesity-related metabolic dysfunction through both thermogenic and non-thermogenic means. However, substantial evidence indicates that obesity negatively affects BAT mitochondrial morphology and oxidative capacity, impairing systemic energy homeostasis. Motivated by this apparent contradiction, we investigated the relationship between obesity and mitochondrial dynamics, as the underlying mechanisms remain incompletely understood. Here, we identified E4BP4 as a transcriptional repressor that prevents obesity-induced mitochondrial fragmentation and oxidative dysfunction by inhibiting ceramide synthesis in brown fat. Specifically, E4BP4 interacts with PRDM16 to repress Cers6 mRNA expression and consequently reduces C16:0 ceramide levels by binding to a 65 kb upstream enhancer region of the Cers6 gene. Notably, the preservation of mitochondrial integrity in BAT by E4BP4 gain-of-function improves systemic glucose homeostasis, independent of weight loss. Collectively, our findings establish E4BP4 as a molecular safeguard against obesity-induced mitochondrial fragmentation and oxidative dysfunction, primarily by suppressing ceramide synthesis in brown fat.

KEYWORDS

Obesity, Brown Adipose Tissue, Mitochondrial Dynamics, Transcription Factors, Ceramides.

INTRODUCTION

BAT is a metabolically active adipose depot characterized by high mitochondrial density and the capacity to dissipate energy as heat via uncoupling protein 1 (UCP1)-dependent and UCP1-independent mechanisms[1,2]. Numerous rodent studies have demonstrated that BAT-mediated non-shivering thermogenesis enhances whole-body energy expenditure, promotes weight loss, and counteracts obesity-related metabolic diseases[3]. However, whether BAT-induced thermogenesis significantly improves human systemic energy homeostasis remains debatable[4]. Emerging evidence suggests that BAT may influence systemic glucose homeostasis in non-thermogenic ways[3]. For example, BAT facilitates the catabolism of branched-chain amino acids (BCAAs), supplying nitrogen for hepatic biosynthesis of essential amino acids and glutathione[5]. Impaired BCAAs flux and catabolism within BAT mitochondria have been associated with insulin resistance independent of changes in energy expenditure or body weight[5]. Regardless of whether it is through non-shivering thermogenesis or other means, maintaining mitochondrial health is crucial for BAT's beneficial effects on systemic energy homeostasis.

Given the central role of mitochondrial integrity in BAT function, understanding how mitochondrial morphology is regulated under metabolic stress is essential. Changes in mitochondrial architecture through fusion and fission events, collectively termed mitochondrial dynamics, represent adaptive responses to an organism's energy supply and demand, directly influencing mitochondrial oxidative capacity[6]. Studies have indicated that obesity leads to an imbalance in mitochondrial dynamics, favoring fission events that result in mitochondrial fragmentation and reduced oxygen consumption in the liver[7], muscle[8], and in white adipose tissue (WAT)[9]. Mechanistically, recent evidence has demonstrated that obesity induces the expression and activity of RalA, a GTPase family protein, in WAT, driving Drp1-mediated mitochondrial fragmentation[9]. Ablation of RalA in WAT prevents weight gain and enhances fatty acid oxidation in diet-induced obese (DIO) mice. Interestingly, BAT mitochondrial morphology was unaffected by RalA activity, suggesting distinct regulatory mechanisms of mitochondrial morphology related to brown fat.

90 One potential upstream regulator of mitochondrial morphology during
91 obesity is the accumulation of ceramides, which have emerged as key lipids in
92 metabolic disease. Ceramides are bioactive sphingolipids that accumulate in
93 various tissues during obesity, contributing significantly to cardiometabolic
94 diseases, including type 2 diabetes, hepatic steatosis, and atherosclerosis[10-17].
95 Numerous pharmacological and genetic interventions in rodents have
96 demonstrated that inhibiting *de novo* ceramide synthesis in adipose tissue
97 improves systemic energy homeostasis[16,18-22]. Furthermore, ceramide
98 accumulation is sufficient and necessary to disrupt BAT thermogenic function and
99 cause metabolic dysfunction in DIO mice[19].

100 Among various ceramide species, C16:0 ceramide has garnered particular
101 attention due to its direct impact on mitochondrial morphology and oxidative
102 metabolism. C16:0 ceramide buildup within BAT is associated with altered
103 mitochondrial morphology and decreased mitochondrial respiration[19]. C16:0
104 ceramide synthesis is mediated by the enzymatic activity of ceramide synthase
105 (Cers) isoforms 5 and 6[23]. In a large human cohort study, visceral WAT expression
106 of Cers6 was positively correlated with higher body mass index (BMI), fat
107 accumulation, and hyperglycemia[16]. Moreover, conditional deletion of Cers6,
108 specifically in UCP1+ cells, enhances BAT thermogenic capacity and improves
109 systemic energy homeostasis in DIO mice[16]. Several distinct mechanisms have
110 been proposed, through which C16:0 ceramide influences mitochondrial
111 morphology and oxidative capacity[17]. For instance, C16:0 ceramide directly
112 interacts with mitochondrial fission factor (Mff), thus promoting Drp1-dependent
113 mitochondrial fragmentation in hepatocytes[7]. Notably, hepatic deficiency of
114 CerS6, but not CerS5, confers protection against weight gain, hepatic lipid
115 accumulation, insulin resistance, and impaired mitochondrial oxidative function in
116 DIO mice[7].

117 Despite substantial evidence linking obesity-induced ceramide
118 accumulation to mitochondrial damage in BAT, the underlying mechanism
119 remains unclear. In this study, we identified E4 promoter-binding protein 4
120 (E4BP4), a member of the proline- and acid-rich (PAR) family of transcription
121 factors, as a critical safeguarding factor against obesity-induced mitochondrial
122 fragmentation, thereby preserving the mitochondrial oxidative capacity. E4BP4 is

co-regulated by PRDM16 and directly represses Cers6 expression, leading to decreased C16:0 ceramide levels. Notably, ceramide repression by the E4BP4-PRDM16 transcriptional complex significantly improved systemic glucose homeostasis independent of body weight loss. These findings enhance our understanding of brown fat biology and shed light on the molecular mechanisms underlying obesity-induced mitochondrial damage.

RESULTS

E4BP4 is a transcription factor repressed in BAT of diet-induced obesity (DIO) mice.

Although considerable advances have elucidated the roles of various transcription factors (TF) in the differentiation of brown and beige adipocytes as well as in the activation of thermogenic program, our understanding of TF functions in metabolic disorders remains unclear. Thus, to identify TF candidates that may be relevant in obesity, we analyzed public bulk RNA-seq datasets from interscapular BAT (iBAT) of chow-fed and DIO mice[24]. We investigated 289 curated TF **(Table 1)** previously identified in iBAT, using mass spectrometry[25]. Among the top ten downregulated TF in DIO versus chow diet mice, several were previously linked to brown and beige adipocyte development and the activation of thermogenic genes, including Nra4a1, Arntl1 (Bmal1), Zbtb16, and Ebf1[26-29] **(Figure 1A)**. E4bp4 caught our attention because it is a basic leucine zipper (bZIP) transcription factor that contains a unique repressor domain[30] **(Figure 1B)**. Moreover, single nucleotide polymorphisms of E4bp4 were strongly associated (HuGE scores) with a higher body mass index (8.59 -log10 p-value), waist-to-hip ratio (6.39 -log10 p-value), and weight (12.86 -log10 p-value), based on GWAS studies derived from the Type 2 Diabetes Knowledge Portal (https://t2d.hugeamp.org/) **(Figure 1C)**.

E4BP4, also known as nuclear factor interleukin 3 regulated (Nfil3), belongs to the PAR subfamily of bZIP proteins, which includes DBP, HLF, and TEF[31]. It was originally described as a repressor that binds to a consensus sequence in the adenoviral E4 promoter[32]. Additionally, E4bp4 is an established component of the mammalian circadian clock, and prior findings suggest it may affect energy balance and metabolism[33,34]. However, its role in BAT remains

155 unknown. To determine whether E4bp4 is suppressed by high-fat feeding, mice
156 were fed an HFD for either one or ten weeks. After one week, E4bp4 mRNA
157 levels remained unchanged, but after ten weeks, they were 54% reduced
158 compared to the control **(Figure 1D)**.

159 **E4BP4 expression is induced by cold stimulus and adrenergic signaling in**
160 **brown fat**

161 To investigate the regulation of E4bp4 in brown fat, we first analyzed
162 publicly available iBAT bulk RNA-seq datasets[35] from mice exposed to acute cold
163 for 8h. The analysis revealed that E4bp4 expression, along with thermogenic
164 genes (Ucp1, Dio2, Elovl3, Ppargc1α and Ppargc1β) were induced in mice under
165 cold versus thermoneutrality (TN) **(Figure 1E)**. Alternatively, we performed gene
166 expression analysis of iBAT in mice acutely (6h and 12h) or chronically (1-14
167 days) exposed to cold stress (4°C). As a control, mice were kept under TN. Our
168 results confirmed that E4bp4 mRNA levels were higher in iBAT of mice under both
169 acute and chronic cold exposure than in the control **(Figure 1F)**.

170 To determine whether E4bp4 expression is mediated by β-adrenergic
171 receptor (βAR) signaling, we treated immortalized brown adipocytes with the non-
172 selective βAR agonist isoproterenol (ISO) for 24h. In this context, previous study
173 has suggested that E4BP4 may play a role in cAMP-induced beige adipocyte
174 differentiation[36]. Our results revealed an increase in E4bp4 mRNA levels **(Figure**
175 **1G)** and protein content **(Figure 1H)** in ISO compared to vehicle-treated cells.
176 We also examined the regulation of E4bp4 expression in human brown
177 adipocytes. The cells were treated with forskolin, an adenylate cyclase activator.
178 Forskolin-treated human brown adipocytes had higher E4BP4 mRNA levels
179 **(Figure 1I)** and protein content **(Figure 1J)** than those in the control group. Taken
180 together, these data reveal that E4BP4 is induced in brown adipocytes by both
181 cold stress and βAR signaling.

182 **E4BP4 overexpression (OE) prevented HFD-induced metabolic dysfunction**

183 Next, we induced E4bp4 overexpression (E4bp4-OE) by injecting an
184 adeno-associated vector (AAV) into the iBAT. AAV-GFP was used as the control.
185 Mice were fed a HFD for 10 weeks at TN (28-29°C). The rationale for using this
186 model was to provide housing conditions that closely resemble those of humans

187 with minimal or no cold-induced thermogenesis[37]. Moreover, transgene
188 expression by local AAV administration into brown fat is an alternative strategy to
189 circumvent issues recently reported in the Ucp1 Cre mouse lineage, such as
190 genetic abnormalities[38] and non-adipose tissue transgene expression[39,40]. iBAT
191 temperature was recorded using a thermal probe (IPTT300) throughout the 10
192 weeks of HFD feeding **(Figure S1A)**. Our data revealed no differences in body
193 weight **(Figure S1B)** or food intake **(Figure S1C)** between the two groups.
194 Nonetheless, the iBAT temperature remained consistently higher in the E4BP4-
195 OE group throughout the HFD feeding period **(Figure S1D)**. AAV E4bp4
196 administration increased E4bp4 mRNA levels 63 fold compared to that in the
197 control group **(Figure S1E)**.

198 Next, we investigated the effects of E4bp4 gain-of-function on brown fat
199 mass and morphology. iBAT mass was lower in the E4BP4 group than in the
200 control group **(Figure S1F)**. Histological analysis using hematoxylin and eosin
201 (H&E) staining revealed a white adipocyte-like phenotype characterized by
202 unilocular and large adipocytes in the control group. Conversely, E4BP4
203 displayed a typical multilocular morphology, with smaller adipocytes **(Figure**
204 **S1G)**. Moreover, immunofluorescence assay of an outer mitochondrial
205 membrane protein (TOM20) revealed higher mitochondrial content in E4BP4 than
206 in the control **(Figure S1H)**.

207 Studies have demonstrated that E4BP4 is crucial for controlling the
208 development and activity of immune cells[41]. Therefore, to avoid E4BP4 indirect
209 effects on resident immune cells within iBAT, we next induced E4bp4 transgene
210 expression using AAV under the control of the adiponectin promoter. In the first
211 cohort, mice were fed an HFD for two weeks at TN (28-29°C), followed by indirect
212 calorimetry **(Figure 2A)**. This short-term HFD protocol minimizes the extensive
213 iBAT remodeling (*whitening)* commonly observed in longer DIO studies[42,43]. We
214 found increased energy expenditure (EE) in E4BP4-OE **(Figure 2B)**, with no
215 differences in body weight **(Figure S2A)** or tissue mass **(Figure S2B)**. Moreover,
216 the oxygen consumption rate (OCR) of iBAT was higher in the E4BP4-OE group
217 **(Figure 2C)**. E4bp4 mRNA was upregulated 46-fold relative to the control **(Figure**
218 **2D)**.

219 In the second cohort, mice were exposed to a longer 10 weeks of HFD
220 under TN (28-29°C) **(Figure 2E)**. Consistent with our earlier findings **(Figure**
221 **S1B)**, body weight did not differ between the groups **(Figure 2F)**. Interestingly,
222 our data revealed a slight but significant increase in food intake in the E4BP4
223 group **(Figure 2G)**. To further investigate the effects of the E4BP4 gain-of-
224 function on glucose homeostasis, we performed glucose (GTT) and insulin (ITT)
225 tolerance tests in both groups after 10 weeks of HFD feeding. Our data
226 demonstrated a significant improvement in glucose tolerance **(Figure 2H)** and
227 insulin sensitivity **(Figure 2I)** in E4BP4 compared with the control.

228 No differences were observed in subcutaneous inguinal adipose tissue
229 (iWAT), liver, muscle, or heart mass between the two groups. In contrast, we
230 found lower iBAT and gonadal adipose tissue (gWAT) mass for E4BP4 than for
231 the control **(Figure S2C)**. We observed increased iBAT E4bp4 mRNA levels
232 **(Figure 2J)** and protein content **(Figure 2K)**. It is worth noting that no E4bp4
233 transgene expression was detected in iWAT, gWAT, liver, or muscle
234 (gastrocnemius) **(Figure S2D).** Similar to our earlier observations **(Figure S1G)**,
235 H&E staining of iBAT from E4BP4 exhibited a multilocular morphology with
236 smaller adipocytes than those in the control **(Figure S2E)**. Finally, the iBAT OCR
237 remained significantly higher in E4BP4-OE than in the control **(Figure 2L)**.
238 Collectively, our data demonstrate that E4BP4 gain-of-function improves
239 systemic energy homeostasis that is associated with changes in BAT
240 mitochondrial content and oxidative capacity.

241 **E4BP4 prevents obesity-induced mitochondria fragmentation in brown fat**

242 To understand how E4BP4 gain-of-function sustains higher brown fat
243 mitochondrial content in DIO mice, we first analyzed publicly available single-cell
244 RNA-sequencing datasets of iBAT. Our data revealed that the expression of
245 E4bp4 was enriched in the brown adipocyte subpopulation along with Ucp1 and
246 other genes related to the thermogenic program **(Figure S2F)**. Therefore, we
247 investigated whether E4bp4-OE induces mitochondrial biogenesis. However, we
248 observed no differences in the mRNA levels of thermogenic or mitochondrial
249 biogenesis genes such as Ucp1, Prdm16, Tfam, Nrf1, or Ppargc1α between the
250 two groups **(Figure S2G)**.

251 Obesity leads to an imbalance in mitochondrial dynamics, favoring fission
252 events that result in fragmented mitochondria[9]. Fragmented and depolarized
253 mitochondria activates mitophagy, leading to reduced mitochondria mass[6]. Thus,
254 we explored whether E4BP4 gain-of-function prevents HFD-induced
255 mitochondrial fragmentation in iBAT. Samples from the DIO mice, as described in
256 Figure 2E, were subjected to transmission electron microscopy analysis. Our data
257 demonstrated the appearance of smaller spherical mitochondria in the control
258 group, which suggests more fragmented mitochondria[7,9]. In contrast, E4bp4 gain-
259 of-function led to a higher frequency of elongated mitochondria **(Figures 3A –**
260 **3C)**. Next, we investigated whether E4BP4 controls mitochondrial morphology in
261 a *cell-autonomous* manner. E4bp4-OE was induced via AAV transduction, with
262 AAV-GFP serving as the control in primary brown adipocytes **(Figure S3A)**. As
263 expected, E4bp4-OE led to a higher E4bp4 protein content **(Figure S3B)**, with no
264 effects on brown adipogenesis, compared to the control **(Figure S3C)**. Lipid
265 overload was induced *in vitro* by pretreating cells with palmitate (500 μM) for 24h
266 and performing immunofluorescence analysis **(Figure 3D)**. Confocal imaging
267 revealed fewer fragmented mitochondria in E4bp4-OE cells than in the control
268 **(Figure 3E)**. Notably, no changes in the mitochondrial-to-nuclear DNA ratio were
269 observed **(Figure S3D)** between the groups, which is consistent with our earlier
270 data **(Figure S2G),** suggesting no induction of mitochondrial biogenesis by
271 E4bp4 in DIO mice.

272 Alternatively, to investigate mitochondrial dynamics, we also used brown
273 adipocytes derived from a previously established photo-activatable mitochondria
274 (PhAM) reporter mouse model. PhAMfl/fl mice were crossed with adiponectin-
275 Cre (AdipoQ-Cre) mice to drive conditional expression of the fluorescent protein
276 Dendra2 specifically in adipocytes **(Figure 3F)**. Dendra2 fluoresces green under
277 baseline conditions but irreversibly switches to red fluorescence upon activation
278 with a 405 nm laser. This enables tracking of mitochondrial fusion events by
279 assessing the co-localization of pre-existing (green) and newly photo-activated
280 (red) mitochondria. The iBAT was collected from these mice, and the stromal
281 vascular fraction (SVF) was isolated and differentiated into brown adipocytes,
282 which retained green-fluorescent mitochondria. Cells were then pre-treated with
283 palmitate (500 μM) for 24 hours, followed by time-lapse microscopy **(Figure 3F)**.

Our results showed that palmitate treatment induced mitochondrial fragmentation in brown adipocytes, an effect that was prevented by E4BP4-OE **(Figure 3G; Video S1)**. Notably, in vehicle-treated cells, we observed no increase in colocalized mitochondria in E4BP4 cells compared with the control. These findings suggest that the higher mitochondrial colocalization in the E4BP4 group is a consequence of fewer fission events than of higher fusion events.

We also evaluated whether the E4bp4 gain-of-function affects mitochondrial membrane potential (ΔΨm) of brown adipocytes. To this end, we used a combination of MitoTracker Green (MTG) and tetramethylrhodamine ethyl ester (TMRE) as previously reported[44]. Primary brown adipocytes were pretreated with palmitate (500 μM) for 24 h. After a washout period, we co-stained brown adipocytes with MTG and TMRE and reintroduced the palmitate-containing medium, followed by time-lapse microscopy **(Figure 3H)**. Our findings revealed that the control cells experienced a noticeable decrease in ΔΨm within 2 min. In contrast, cells overexpressing E4bp4 maintained their ΔΨm for up to one hour **(Figure 3H)**. Finally, we explored whether E4bp4 sustained ΔΨm could be translated into preserved mitochondrial oxidative function by performing an OCR analysis. Following pretreatment with palmitate (6h or 24h), we observed a modest but significant increase in both basal and norepinephrine-stimulated OCR in E4bp4-overexpressing cells compared with the control. Notably, E4bp4-OE elicited a robust increase in the maximal OCR induced by FCCP **(Figure 3I)**. It is worth noting that a substantial proportional change in maximal OCR, exceeding that observed for other parameters, is likely attributable to enhanced mitochondrial substrate oxidation capacity, with alterations in mitochondrial uncoupling as a secondary consequence[45]. Overall, our data demonstrated that E4bp4 gain-of-function preserved brown fat ΔΨm and oxidative capacity by preventing mitochondrial fragmentation induced by lipid overload.

E4BP4 OE suppress ceramide synthesis in brown fat

To investigate the underlying mechanisms, we conducted bulk RNA sequencing (RNA-seq) on iBAT samples obtained from the experiments shown in **Figure S1A**. Our differential gene expression analysis demonstrated that 722 and 217 genes were upregulated and downregulated, respectively **(Table 2)** in E4BP4 compared with those in the control. Enrichment pathway analysis (KEEG)

317 revealed that “sphingolipids” was the most significantly downregulated pathway
318 **(Figure 4A)**. These findings have caught our attention because sphingolipids,
319 particularly ceramides, have been shown to induce cellular and systemic
320 metabolic dysfunction, by affecting mitochondria oxidative capacity[46]. Heatmap
321 analysis demonstrated that the genes related to *de novo* synthesis of ceramides
322 as well as “recycling pathways” were the most repressed genes in E4BP4
323 compared to the control **(Figure 4B)**. To further investigate whether the
324 decreased expression of ceramide biosynthetic genes might result in decreased
325 sphingolipid levels, we performed mass spectrometry analysis of the
326 “sphingolipidome” of iBAT from the experiments described in **Figure 2E**. Our data
327 demonstrated that E4bp4 OE led to lower levels of C16:0 ceramide with no
328 changes in other ceramide molecules **(Figure 4C)**. Interestingly, we also
329 observed an increase in the levels of other sphingolipid molecules, such as
330 hexosylceramide (HexCer), sphingomyelin (SM), and lactosylceramide (LacCer),
331 in E4BP4 compared to those in the control **(Figure 4C)**.

332 Next, to investigate whether E4BP4 modulates sphingolipid abundance in
333 a cell-autonomous manner, we performed sphingolipidome analysis of primary
334 brown adipocytes pretreated with palmitate (500 μM) for 24h. Our data revealed
335 decreased long-side chain (C16:0, C18:0, C20:1, and C22:5) ceramides, with no
336 changes in HexCer, SM, and LacCer (except HexCer 20:4, HexCer 22:6, and
337 dihydroceramide 22:1) in E4BP4-OE relative to the control **(Figure 4D)**. Finally,
338 we investigated whether the inhibition *of de novo* ceramide synthesis could
339 prevent palmitate-induced mitochondrial fragmentation in brown adipocytes.
340 Cells were pretreated with myriocin, an inhibitor of the first and rate-limiting step
341 enzymes serine palmitoyltransferase (Sptlc) isoforms 1 and 2 **(Figure 4E)**. Our
342 data showed that myriocin prevented palmitate-induced mitochondrial
343 fragmentation in brown adipocytes **(Figure 4F)**. Taken together, these findings
344 suggest that the inhibition *of de novo* ceramide synthesis is sufficient to prevent
345 lipid overload-induced mitochondrial fragmentation in brown adipocytes.

346 **E4BP4 mitigates Drp1-induced mitochondrial fragmentation by repressing**
347 **ceramide synthase 6 (Cers6) and *de novo* C16:0 ceramide synthesis in**
348 **brown adipocytes.**

349 Numerous studies have demonstrated that ceramide accumulation leads
350 to reduced mitochondrial oxidative capacity in adipocytes[16,18,19,47]. Of particular
351 interest is C16:0 ceramide, which is derived from the enzymatic activity of Cers5
352 and Cers6. C16:0 ceramide is a well-known sphingolipid that exerts deleterious
353 effects on mitochondrial oxidative function[48]. Therefore, we investigated whether
354 E4bp4 gain-of-function affects Cers6 expression and C16:0 ceramide levels in
355 iBAT of DIO mice. Accordingly, E4bp4-OE decreased Cer6 mRNA levels **(Figure**
356 **5A)** and C16:0 ceramide content compared to those in the control **(Figure 5B)**.
357 Next, we employed E4bp4 gain-of-function *in vitro* to analyze *cell-autonomous*
358 repression of C16:0 ceramide synthesis in brown adipocytes. Again, we observed
359 a decrease in Cers6 mRNA levels **(Figure 5C)** and a reduction in C16:0 ceramide
360 content **(Figure 5D)** in palmitate-treated brown adipocytes of the E4BP4 group
361 compared with the control. Ceramides can be formed via *de novo* synthesis or
362 recycling pathways involving sphingomyelin[49]. Hence, to further investigate
363 whether the decreased C16:0 ceramide levels were related to the repression of
364 *de novo* synthesis of ceramides, we pretreated brown adipocytes with a stable
365 palmitic acid ($^{13}C_{16}$) isotope (500μM) for 6h and monitored the synthesis of C16:0
366 ceramides using mass spectrometry **(Figure 5E)**. Accordingly, E4bp4-OE
367 reduced *de novo* synthesis of C16:0 ceramide compared to that of the control
368 **(Figure 5E)**.

369 A previous study demonstrated that C16:0 ceramides interact with Mff in
370 hepatocytes leading to Drp1-induced mitochondrial fragmentation[7]. Thus, we
371 tested whether E4bp4 gain-of-function mitigates mitochondrial fission by
372 modulating Drp1 activity in primary brown adipocytes **(Figure 5F)**. Cells were
373 pretreated with palmitate (500 μM) for 24h. Our data revealed that E4bp4-OE
374 enhanced phosphorylation of $Drp1^{637}$, an inhibitory residue, leading to decreased
375 Drp1-mediated mitochondrial fission **(Figure 5G)**. Collectively, our data
376 demonstrated that E4bp4 represses Cers6 expression and C16:0 ceramide
377 levels, which in turn prevents mitochondrial fragmentation by reducing Drp1
378 activity in brown adipocytes.

379 **E4BP4 is a DNA-binding TF that represses Cers6 by binding to a 65kb**
380 **upstream enhancer.**

381 We sought to determine whether E4bp4 acts as a DNA-binding TF
382 mediating the repression of Cers6 in brown adipocytes. Hence, we used site-
383 directed mutagenesis to alter the amino acid sequence of the E4bp4 bZIP DNA-
384 binding domain, that is, the mutant (EM) E4bp4 **(Figure 5H)**. Our data revealed
385 the loss of Cers6 repression by overexpression of EM E4bp4 in immortalized
386 brown adipocytes, suggesting that E4bp4 acts as a *bona fide* DNA-binding TF
387 **(Figure 5H)**.

388 Next, we explored whether E4bp4 represses Cers6 mRNA expression by
389 directly binding to its regulatory regions. To this end, we analyzed publicly
390 available ATAC-seq and RNA-seq datasets of brown adipocytes using a machine
391 learning-based approach, "*Integrated analysis of motif activity and gene*
392 *expression changes of transcription factors* (IMAGE)" [50]. Our analysis identified
393 a unique E4bp4 *motif* located 65kb upstream of the Cers6 transcription start site
394 **(Figure 5I)**. To evaluate the chromatin status of this region, we analyzed histone
395 H3K27 acetylation (H3K27ac) and H3K4 monomethylation (H3K4me1) in brown
396 fat using the ENCODE data[51]. Accordingly, we observed enriched H3K27ac and
397 H3K4me1 histone marks in this regulatory region, suggesting that this is a typical
398 enhancer site **(Figure 5I)**. Moreover, it is worth noting that this enhancer is
399 ENCODE annotated as a distal enhancer "E0697815". Therefore, for simplicity,
400 we describe this enhancer as "E0697815." Finally, to validate the binding of
401 E4bp4 to this enhancer, we performed an E4bp4 ChIP-PCR assay. The IgG assay
402 was used as a control. Our data confirmed the enrichment of E4bp4 in E0697815
403 compared with that in IgG **(Figure 5J)**. Altogether, our data demonstrate that
404 E4bp4 acts as a *bona fide* DNA-binding TF to repress Cers6 expression by
405 binding to a 65kb upstream enhancer.

406 **Deletion of Cers6 upstream enhancer (E0697815) is sufficient to protect**
407 **mitochondria from palmitate-induced fragmentation**

408 Next, we evaluated the extent to which E0697815 regulates Cers6
409 expression and C16:0 ceramide levels. To this end, CRISPR/Cas9 was used to
410 alter the genomic sequence of E0697815 in immortalized brown adipocytes
411 **(Figures S3E and S3F)**. Sanger sequencing confirmed the presence of an
412 altered nucleotide sequence in the enhancer region **(Figure S3G)**. Our data
413 revealed that mutant E0697815 (EΔ) was sufficient to reduce Cers6 mRNA levels

414 **(Figure S3H)** and C16:0 ceramide content **(Figure S3I)** in brown adipocytes,
415 suggesting that E0697815 is a relevant enhancer for controlling Cers6
416 expression. Moreover, we investigated whether EΔ affects E4BP4-mediated
417 repression of Cers6 expression. Accordingly, we found that the EΔ of Cers6
418 mitigated E4BP4-induced repression of Cers6 mRNA **(Figure 5K)** and C16:0
419 ceramide levels **(Figure 5L)**.

420 To further investigate whether the E0697815 mutation in Cers6 was
421 sufficient to prevent palmitate-induced mitochondrial fragmentation, we
422 pretreated the EΔ brown adipocytes with 500μM palmitate for 24h. Mitochondrial
423 morphology was investigated using immunofluorescence assay. As expected, the
424 non-edited control cells displayed fragmented mitochondrial morphology. In
425 contrast, the EΔ of Cers6 was sufficient to prevent palmitate-induced changes in
426 mitochondrial morphology of brown adipocytes **(Figure 5M)**. Finally, we
427 conducted OCR analysis to investigate the mitochondrial oxidative capacity in the
428 EΔ Cers6 gene versus non-edited control cells. Brown adipocytes were
429 pretreated with 500μM palmitate for 6 and 24 h before functional analysis. Our
430 data revealed no differences in OCR between EΔ- and control-treated brown
431 adipocytes after 6 h of treatment. However, 24h palmitate treatment significantly
432 decreased OCR at all evaluated respiratory states in the non-edited group, in
433 relation to the EΔ in brown adipocytes. **(Figure 5N)**. Taken together, deletion of
434 the 65kb upstream Cers6 enhancer is sufficient to prevent palmitate-induced
435 mitochondrial fragmentation and decrease oxidative capacity in brown
436 adipocytes.

437 **E4BP4 is co-regulated by PRDM16 to repress Cers6 expression and C16:0**
438 **ceramide levels**

439 Given prior evidence that E4BP4 interacts with PRDM16 in beige
440 adipocytes[52], we sought to determine whether a similar interaction occurs in
441 brown fat. To this end, immortalized brown adipocytes were transfected with Flag-
442 Prdm16 vector, followed by immunoprecipitation. After cell differentiation, Prdm16
443 was pulled down from the cell extracts using a Flag antibody. Our data revealed
444 the presence of endogenous E4bp4 in the Prdm16 complex **(Figure 6A)**.
445 Moreover, we analyzed publicly available Prdm16 ChIP-seq data from iBAT[53].
446 Interestingly, our analysis revealed a Prdm16 binding site at E0697815 of the

447 Cers6 gene. In contrast, the deletion of Prdm16 (Prdm16KO) abolished the peak
448 at E0697815 **(Figure 6B)**.

449 Previous studies revealed that Prdm16 is involved with the transcriptional
450 repression programs in adipocytes[52,54,55]. Therefore, we investigated whether
451 Prdm16 is associated with the transcriptional repression of Cers6 in brown
452 adipocytes. To this end, we used the CRISPR activation (CRISPRa) mouse
453 model previously established by our group[56]. AdipoQ-Cre mice were crossed with
454 CRISPRa (SPH) mice to establish the conditional expression of CRISPRa
455 machinery in adipose tissues (AdipoQ_SPH). Overexpression of endogenous
456 Prdm16 (Prdm16-OE) was achieved using an AAV single guide RNA (sgRNA)
457 targeting Prdm16 **(Figure 6C)**. iBAT was harvested, and SVF was differentiated
458 into brown adipocytes *in vitro*. As expected, Prdm16-OE enhanced the mRNA
459 levels of Prdm16 and thermogenic genes such as Ucp1, Cox8b, Ppargc1α, and
460 Cidea, compared to the control **(Figure 6D)**. Moreover, Prdm16-OE led to
461 decreased Cers6 mRNA levels **(Figure 6E)** and C16:0 ceramide content **(Figure
462 6F)** in palmitate-treated brown adipocytes compared with those in the control.
463 Finally, we investigated whether E4bp4 is necessary for the Prdm16-mediated
464 repression of Cers6 expression. We developed an E4bp4 loss-of-function model
465 by using a lentiviral short hairpin in immortalized brown adipocytes. A scrambled
466 lentiviral sequence was used as the control. Western blot analysis confirmed the
467 loss-of-function of E4bp4 in brown adipocytes **(Figure 6G).** Notably, E4bp4
468 knockdown did not affect brown adipocyte differentiation, as defined by Oil Red
469 O staining **(Figure 6H)** or expression of adipogenic genes **(Figure 6I)**. E4bp4
470 knockdown mitigated the Prdm16-mediated reduction of Cers6 mRNA levels
471 **(Figure 6J)** and C16:0 ceramide content **(Figure 6K)**. Taken together, our data
472 revealed that E4bp4 is co-regulated by Prdm16 to repress Cers6 expression and
473 C16:0 ceramide levels in brown adipocytes **(Figure 6L)**.

474 **DISCUSSION**

475 This study supports a model in which forced E4BP4 expression during DIO
476 prevents mitochondrial fragmentation and oxidative dysfunction in brown fat, at
477 least in part, through repression of ceramide levels in mice. E4BP4 interacts in a
478 transcriptional complex with PRDM16 and directly represses Cers6 mRNA
479 expression and C16:0 ceramide levels by binding to a 65kb upstream Cers6

480 enhancer. Reduction of Cers6- derived C16:0 ceramide through E4BP4
481 overexpression or ablation of the Cers6 upstream enhancer was sufficient to
482 prevent palmitate-induced mitochondrial fragmentation and oxidative
483 dysfunction. Notably, the preservation of BAT mitochondrial health by E4BP4
484 gain-of-function is sufficient to improve systemic glucose homeostasis,
485 independent of weight loss.

486 E4BP4 is a member of the PAR-bZIP family of transcription factors,
487 characterized by a unique transcriptional repression domain comprising
488 approximately 65 amino acids (residues 299–363) near its C-terminus[32]. Studies
489 using fusion proteins have demonstrated that this specific domain independently
490 acts as a transcriptional repressor when coupled to a heterologous protein, such
491 as the yeast GAL4 DNA-binding domain[30]. These findings prompted us to
492 investigate the transcriptional repression role of E4BP4 in brown fat. In this study,
493 we found that E4BP4 acts as a *bona fide* transcription factor, as evidenced by a
494 mutation in its bZIP domain that disrupts transcriptional repression of Cers6.
495 Recently, the crystal structure of the E4BP4 bZIP domain was elucidated,
496 revealing an α-helical structure that forms dimers via its leucine zipper region and
497 preferentially interacts with the TTACGTAA DNA *motif*[31]. Notably, disease-
498 associated mutations within the E4BP4's bZIP domain impair or completely
499 abolish its DNA binding capacity[31]. Additionally, it has been demonstrated that
500 E4BP4 mediates transcriptional repression by recruiting the TBP-binding protein
501 Dr1[57]. However, the mechanisms by which E4BP4 represses Cers6 mRNA
502 remain to be fully elucidated.

503 We found that E4BP4 is guided by PRDM16 to repress Cers6 mRNA levels
504 by binding to an enhancer region located 65 kb upstream of the gene (E0697815).
505 Notably, the E0697815 mutation abolished the repression of Cers6 mRNA
506 mediated by the E4BP4-PRDM16 complex in brown adipocytes. Furthermore,
507 E4BP4 is necessary for the PRDM16-mediated suppression of both Cers6 mRNA
508 levels and C16:0 ceramide content. These observations reinforce the concept
509 that PRDM16 acts not only as a critical regulator of the thermogenic gene
510 program but also as a broader co-regulator involved in repressing several
511 biological pathways[58]. For example, PRDM16 interacts with GTF2IRD1, a
512 member of the TFII-I family of DNA-binding proteins, to inhibit collagen

513 expression and fibrosis development in adipose tissue[52]. The PRDM16 protein
514 has a short half-life[59,60]. In this regard, a recent study identified the CUL2-
515 APPBP2 complex as the ubiquitin E3 ligase responsible for controlling PRDM16
516 stability through polyubiquitination[61]. Inhibition of the CUL2-APPBP2 complex
517 extends the half-life of PRDM16 and mitigates obesity-related metabolic
518 dysfunction[61]. E4BP4 is also tightly regulated at post-translational level[62,63].
519 However, whether E4BP4 protein half-life can also be extended by inhibition of
520 the CUL2-APPBP2 complex is a matter for future investigation.

521 Excess nutrients impair mitochondrial oxidative phosphorylation in various
522 cell types, including muscle and pancreatic beta cells[6]. However, it has been
523 hypothesized that under conditions where ATP demand is not the primary driver
524 of oxygen consumption, such as during increased mitochondrial uncoupling in
525 activated brown adipocytes, the negative impact of excess nutrients on
526 mitochondrial oxidative capacity could be minimal[6]. Nevertheless, our findings
527 demonstrated that lipid overload induces mitochondrial fragmentation and
528 oxidative dysfunction in brown fat, at least in part, through the accumulation of
529 C16:0 ceramide. Importantly, the subcellular localization of Cers6 significantly
530 influences mitochondrial morphology and oxidative function, as it is positioned at
531 mitochondria and mitochondria-associated membranes[48]. This localization
532 facilitates the interaction between C16:0 ceramide and Mff, which subsequently
533 activates Drp1-mediated mitochondrial fragmentation[7]. Consistent with these
534 observations, hepatic deletion of Cers6, but not Cers5, improves systemic energy
535 homeostasis in DIO mice[7]. However, it remains possible that reducing C16:0
536 ceramide levels may enhance the mitochondrial oxidative capacity in brown fat
537 through mechanisms other than regulating mitochondrial morphology. For
538 instance, C16:0 ceramide may affect mitochondrial function by acting on electron
539 transport chain complexes[47,64]. Moreover, recent studies[65,66] have identified
540 C16:0 ceramide as a ligand for cell membrane G protein-coupled receptors.
541 C16:0 ceramide binds to FPR2, inhibiting thermogenesis via the Gi-cyclic AMP
542 signaling pathway, thereby reducing whole-body energy expenditure[66]. Thus,
543 these are distinct yet non-mutually exclusive mechanisms by which C16:0
544 ceramide can impair mitochondrial oxidative capacity in adipose tissue.

One of the main findings of our study was that preserving BAT´s mitochondrial morphology and oxidative capacity through E4BP4 gain-of-function improves glucose homeostasis in DIO mice, independent of weight loss. However, we cannot rule out that enhanced energy expenditure plays a role in the improvement of glucose homeostasis, as E4BP4 gain-of-function increases the iBAT temperature and whole-body energy expenditure in DIO mice. The absence of changes in body weight and composition may be explained by a compensatory increase in food intake in the E4BP4 group. Interestingly, these findings align with previous large epidemiological studies, which demonstrated that individuals with detectable BAT had lower circulating glucose levels and approximately a 50% reduced risk of developing type 2 diabetes, irrespective of body weight differences related to their counterparts[67]. Furthermore, interventional studies have shown that activation of BAT using mirabegron, a selective β_3AR agonist, significantly improves glucose homeostasis markers in both healthy[68] and obese insulin-resistant individuals[69], independent of changes in body weight. These findings reinforce the notion that BAT improves systemic energy homeostasis through mechanisms that extend beyond its classical role of increasing energy expenditure and body weight loss. Therefore, preserving mitochondrial integrity and oxidative capacity should be a primary goal for therapeutic strategies targeting obesity-related metabolic diseases.

Limitations of the study

We acknowledge the limitations of our lipidomic approach, particularly regarding the analysis of sphingolipids. While our untargeted analysis provided a broad overview of lipid species present in the samples, it may not have fully captured the diversity of sphingolipids, such as sphingomyelins, dihydroceramides, sphingosine, sphinganine, sphingosine-1-phosphate, ceramide-1-phosphate, and gangliosides. To address this, we performed a targeted lipidomic analysis focused on C16:0 ceramide, which was consistently detected across replicates. The downregulation of C16:0 ceramide explains the preservation of mitochondrial morphology (less fragmented) and oxidative capacity observed with the E4BP4 gain-of-function. We also recognize that E4BP4 could improve systemic glucose homeostasis through mechanisms beyond the regulation of ceramide levels.

577 Lastly, we did not examine the effects of E4BP4 in female mice, and the possibility
578 of sexual dimorphism remains to be explored in future studies.

579

580

581

582

RESOURCE AVAILABILITY

Lead contact

Further information and requests for resources and reagents should be directed to and will be fulfilled by lead contact, Carlos Henrique Grossi Sponton (csponton@usp.br).

Materials availability

Materials generated in this study are available upon request from the lead contact.

Data and code availability

- Any additional information required to reanalyze the data reported in this work paper is available from the lead contact upon request.
- Supplementary material and uncropped Western Blots are available in Data S1-2.
- This paper does not report original code.
- RNA-seq data have been deposited at GEO and publicly available as of the date of publication.

ACKNOWLEDGMENTS

We thank Joseane Morari, Marcio Cruz, Erika Roman, and Gerson Ferraz, from the University of Campinas for technical assistance. We thank National Institute of Science and Technology on Photonics Applied to Cell Biology (INFABIC) and Centro Multidisciplinar para Investigação Biológica na Área da Ciência em Animais de Laboratório (CEMIB). We thank the staff of the Life Sciences Core Facility (LaCTAD) from State University of Campinas (UNICAMP) for the genomic analysis. We thank Guilherme Cebinelli from Plataforma de Citometria de fluxo do Hospital Albert Einsten for the Cell sorting analysis. This work used resources of the Centro Nacional de Processamento de Alto Desempenho em São Paulo (CENAPAD-SP). This work was supported by the São Paulo Research Foundation (2020/14725-0, 2020/06057-8, 2021/08354-2, 2013/07607-8, and 2019/15025-5).

613 **AUTHOR CONTRIBUTIONS**

614 Conceptualization, F. V. R. and C.H.S.; investigation, V.O.F., C.E.L., A.M.Z.,
615 M.K.C., F.C.G., A.S., L.R.F., G.L.S., T.G.; writing – original draft, F. V. R. and
616 C.H.S.; writing – review and editing, P.M.M.V., R.F.C., M.A.M., and L.A.V.; funding
617 acquisition, C.H.S. and L.A.V.; supervision, C.H.S.

618 **DECLARATION OF INTERESTS**

619 The authors declare that they have no conflicts of interest.

620 **DECLARATION OF GENERATIVE AI AND AI-ASSISTED TECHNOLOGIES**

621 The authors declare no use of generative AI- or AI-assisted technologies in the
622 writing, editing, or data interpretation processes of this manuscript.

623 **SUPPLEMENTAL INFORMATION**

624 **Document S1.** Figures S1–S3 and Table S1.

625 **Document S2.** Uncropped Western Blots and Electrophoresis Gels.

626 **Table 1.** FPKM-based quantification of expression changes of transcription
627 factors in interscapular brown adipose tissue (related to Figure 1A).

628 **Table 2.** Differential gene expression of cold vs thermoneutrality (related to Figure
629 1E).

630 **Table 3.** Differential gene expression of Control vs E4BP4-OE (related to Figure
631 4).

632 **Video S1.** Live-cell fluorescence of MitoDendra2 in primary brown adipocytes
633 (related to Figure 3G).

634

635

636

637

638

639

640 **EXPERIMENTAL MODEL AND STUDY PARTICIPANT DETAILS**

641 **Mouse husbandry**

642 All animal experiments were performed in compliance with protocols approved by
643 the University of Campinas Guide for the Care and Use of Laboratory Animals
644 (protocol CEUA # 6102-1/2022; #6619-1/2025). All mice were housed under a 12
645 h light – 12 h dark cycle. Room temperature mice were housed at 22 °C. Mice
646 kept under thermoneutral conditions were placed inside an incubator maintained
647 at a temperature of 28-29 °C. Mice were fed a standard diet or high-fat diet (HFD;
648 60% kcal from fat) and had free access to food and water. Mice were fasted for 6
649 h prior to metabolic measurements and brown adipose tissue respiration. SPH
650 mice were acquired from Jackson Laboratory (Strain# 031645) and crossed with
651 Adipo-Cre (Jackson Laboratory, Strain# 028020). To generate reporter primary
652 brown adipocytes for mitochondria, B6;129S-Gt(ROSA)2$^{6Sortm1(CAG-}$
653 $^{COX8A/Dendra2)Dcc}$/J (JAX stock #018385) mice were crossed with mice expressing
654 Cre recombinase under the control of the adiponectin (Adipoq) promoter. This
655 breeding strategy yielded mice expressing Dendra2, a photoactivatable protein
656 located in the mitochondria (PhAM) of adipocytes, as well as Cre-negative
657 littermate controls. Genotyping was performed using the specific primers listed in
658 Table S1, and representative PCR gel images are provided in the Supplementary
659 Materials. Male mice were used unless otherwise stated.

660 **Primary cell isolation and culture**

661 Brown adipose tissue (BAT) was dissected and digested with dispase II (Sigma
662 D4693) and collagenase D (Sigma 11088882001) at 37 °C for 25 min with
663 agitation. The stromal vascular fraction (SVF) containing preadipocytes was
664 separated from the mature adipocytes by centrifugation at 700 × g for 10 min.
665 SVF cells were then plated on coated 6 well plates in culture medium containing
666 Dulbecco's modified Eagle's medium (DMEM) (Thermo Fisher, 10569044)
667 supplemented with 10% fetal bovine serum (FBS) and 1% penicillin/streptomycin
668 (P/S) (Gibco, 15140). Immortalized brown preadipocytes kindly donated by Dr.
669 Marcelo Mori (University of Campinas) were maintained in (DMEM)
670 supplemented with 4.5 g/L glucose, 10% FBS, and 1% P/S at 37 °C with 5% CO_2.
671 Brown adipocyte differentiation was induced by treating the confluent

672 preadipocytes with DMEM containing 10% FBS, 0.5 mM isobutylmethylxanthine,
673 125 μM indomethacin, 2 μg/ml dexamethasone, 20 nM insulin, 1 nM T3, and 1
674 μg/ml rosiglitazone. Two days after induction, the cells were switched to
675 maintenance medium containing 10% FBS, 20 nM insulin, 1 nM T3, and 1 μg/ml
676 rosiglitazone. For Adeno-X 293 cells, Lenti-X 293T cells were grown and
677 maintained in DMEM containing 10% FBS and 1% P/S.

678 **Experimental Details**

679 **Plasmid construction and acquisition**

680 To overexpress E4BP4 under a constitutive promoter, the plasmid carrying the
681 GFP protein (Addgene catalog no. 49055) was replaced with the sequence of
682 E4BP4 amplified from the plasmid (Addgene catalog no. 34572) using Platinum
683 SuperFi II DNA Polymerase (Thermo Fisher). After ligation, specific primers from
684 the promoter and E4BP4 sequence were used to confirm insertion. To
685 overexpress E4BP4 under the control of the adiponectin promoter, the sequence
686 of E4BP4 amplified from the plasmid (Addgene catalog no. 34572) using Platinum
687 SuperFi II DNA Polymerase (ThermoFisher) was inserted into the MCS region of
688 pAAV-ADP-MCS-FLAG (Addgene catalog no. 192360). After ligation, specific
689 primers from the promoter and E4BP4 sequence were used to confirm insertion.
690 PRDM16 overexpression was achieved using a retroviral plasmid purchased
691 from Addgene (catalog no. 15504).

692 **Lentivirus packaging**

693 For viral production, Lenti-X 293T packaging cells were transfected with DNA
694 constructs using pCMV delta R8.2 (Addgene, catalog no.12263) and pMD2.G
695 (Addgene, catalog no. 12259) using polyethylenimine (Sigma-Aldrich, 408727).
696 After 48 h, the viral supernatant was collected and filtered through a 0.45 mm
697 filter.

698 **Adeno-Associated Virus (AAV) packaging and titration**

699 AAV packaging and titration were performed, as previously described [56]. In brief,
700 AAV was produced by triple transfection of a targeting vector plasmid with
701 pAdDeltaF6 plasmid (Addgene catalog no. 112867) and pAAV2/8 plasmid
702 (Addgene catalog no. 112864) into Adeno-X 293 cells (Takarabio) using

703 polyethylenimine (1 µg/µl) (Sigma-Aldrich, 408727). The cells were collected 72 h
704 post-transfection and purified using an Amicon Ultra-0.5 centrifugal filter (Merck
705 Millipore, UFC510024).

706 **Human brown adipocytes**

707 Human brown preadipocytes were maintained in Dulbecco's modified Eagle's
708 medium F12 (DMEM-F12) supplemented with 4.5 g/L glucose, 10% fetal bovine
709 serum (FBS), and 1% penicillin/streptomycin at 37 ºC with 5% CO2. Brown
710 adipocyte differentiation was performed as previously described[70]. In brief, cells
711 were pretreated with 3.3 nM BMP7 for 6 days prior to induction. Immortalized
712 human preadipocytes were cultured in high-glucose DMEM supplemented with
713 10% FBS and antibiotics at 37°C with 5% CO_2. Upon confluency, differentiation
714 was induced using a defined medium containing insulin, T_3, dexamethasone,
715 IBMX, indomethacin, biotin, and pantothenate. Medium was refreshed every 3
716 days for 12 days. After differentiation, the cells were treated with forskolin (20 µM)
717 or vehicle for 24h.

718 **Gain-of-function in immortalized brown adipocytes**

719 E4bp4 (Addgene, catalog no. 34572) and Prdm16 (Addgene, catalog no. 15503)
720 plasmids were transfected using Lipofectamine 3000 (Thermo Fisher Scientific)
721 according to the manufacturer's protocol. Briefly, preadipocytes at 80%
722 confluence were transfected, and 24 h after transfection, the cells were switched
723 to differentiation medium.

724 **AAV overexpression in primary brown adipocytes**

725 Primary brown adipocytes were infected with AAV expressing E4BP4 ($1x10^{10}$
726 vg/ml) in the presence of polybrene (8 ng/µl) (Sigma-Aldrich, H9268), and 18 h
727 after transduction, the cells were switched to differentiation medium. The
728 analyses were performed on mature adipocytes.

729 **Loss-of-function of E4bp4**

730 The short hairpin (shRNA) sequence was cloned into an Age1- and EcorI-
731 digested PIKO.1 hygro plasmid (Addgene, catalog no. 24150) by annealing oligos
732 sh-E4bp4 described in Table S1. Generation of the sh-E4bp4 cell line using
733 lentiviral transduction. 9B cells were transduced with viral supernatant in the

presence of polybrene (8 ng/µl) (Sigma-Aldrich, H9268). Antibiotic selection with hygromycin was initiated 5 days after transduction.

Genome editing of enhancer of cers6

Five sgRNAs target sites were predicted using the CRISPOR tool available in Genome (https://genome.ucsc.edu). Oligos (Table S1) were annealed and cloned into a BsmBI-digested sg-shuttle-RFP657 vector (Addgene, catalog no. 134968). WT1-KO cells were transduced with viral supernatant in the presence of polybrene (8 ng/µl) (Sigma-Aldrich, H9268). After 5 days of expression, positive cells for RFP were isolated by fluorescence (excitation/emission at 611/657 nm) cell sorting, and individual clones were expanded and tested for loss of function of the enhancer of Cers6 using qPCR. To validate the mutation, we first amplified the enhancer by PCR, and the gel band was subjected to Sanger sequencing. To confirm the mutation, sequencing peaks were analyzed using Edit R[71].

Palmitate treatment

Palmitate treatment was performed as previously described[7]. In brief, 500 µM palmitic acid (Sigma-Aldrich, P0500) was conjugated to 1% (w/v) fatty-acid-free low-endotoxin BSA (Sigma-Aldrich, A8806) in DMEM at 37°C for 25 min. Following this, the cells were incubated with BSA-conjugated PAL or BSA for 6 or 24 h at 37°C with 5% CO_2.

Measurement of c16 flux using stable isotopes

Fully differentiated primary brown adipocytes in a 6-well plate were switched to DMEM containing 1% FBS and 500 µM $^{13}C_{16}$ palmitate:BSA (Sigma-Aldrich, 605573) for 3, 6, and 12 h. Lipids were extracted and analyzed using mass spectrometry. Protein concentration was determined using the Pierce BCA Protein Assay Kit (Thermo Fisher Scientific, 23225) and used to normalize the metabolites.

Measurement of oxygen consumption rate

The oxygen consumption rate (OCR) was measured with the Seahorse XFe Extracellular Flux Analyzer (Agilent) in a 24-well plate, as previously described[19], with some modifications. Briefly, primary brown adipocytes were transduced with AAV-E4BP4 or AAV-GFP, and 18 h later, the cells were switched to differentiation

765 medium. The cells were trypsinized on day 8 and plated into 24-well seahorse
766 plates as previously described. The experiment was performed in seahorse assay
767 media supplemented with 10 mM glucose, 2 mM glutamine, and 1 mM pyruvate.
768 Subsequently, drug injections were administered in the following sequence:
769 noradrenaline (1 μM), oligomycin (5 μM), FCCP (5 μM), and Rotenone +
770 Antimycin (1/2 μM). The same methodology was applied to immortalized brown
771 adipocytes with enhancer mutations.

772 **Immunohistochemistry**

773 Cover slips with fully differentiated adipocytes were fixed using 4% PFA in 0.1 M
774 PBS for 15 min at room temperature. After two PBS washes, the cells were
775 incubated in blocking solution (10% normal donkey serum in 0.1 M PBS
776 containing 0.2% Triton X-100) for 1.5 hours at room temperature. Next, the
777 adipocytes were incubated overnight at 4°C in fresh blocking solution (3% normal
778 donkey serum) containing rabbit anti-TOM20 (1:200; MA5-24859, Thermo Fisher
779 Scientific) without mixing. After three PBS washes, the cells were incubated in a
780 blocking solution containing donkey anti-rabbit FITC (1:500; ab6798 or Ab6941)
781 for 90 min at room temperature. The slides were washed three more times with
782 PBS, mounted, and imaged using a Zeiss LSM880 Airyscan microscope with the
783 ZEN Software (Carl Zeiss). Immunopositive cell counts were averaged from three
784 cover slips per experimental replicate, with 4-5 fields imaged per cover slip.
785 Quantification of immunopositive cells per image was performed using Fiji
786 software, employing the Deconvolution plugin (Deconvolved 3D) for
787 mitochondrial isolation and the Mitochondria Analyzer plugin for quantification.
788 Cells with significant mitochondrial network fragmentation were counted as
789 described previously[7], and image representation was generated from the
790 maximum projection of z-stacks.

791 **High-resolution time-lapse imaging and mitochondrial signal**
792 **quantification**

793 Live-cell super-resolution images were acquired using a Zeiss LSM880 confocal
794 microscope equipped with an Airyscan detector (Carl Zeiss AG, Germany) using
795 a Plan-Apochromat 63×/1.4 oil immersion magnification. All time-lapse
796 acquisitions were conducted under physiological conditions using a stage-top

797 incubation system that maintained cells at 37 °C in a humidified atmosphere with
798 5% CO_2. Dendra2 was excited in its native state using a 488 nm laser line and
799 in its photoconverted state using a 543 nm laser. Photoconversion was induced
800 by illuminating a defined region of interest with a 405 nm laser, 5%, 90 iterations
801 for bleaching, with a scan speed of 6. The time series consisted of 9 cycles with
802 a frame interval of 30 min. The 3D images were 1024 × 1024, 8 bits, zoom 3,
803 resolution 4.8 px/µm. Image analysis was performed using the FIJI/ImageJ
804 software. Single-channel images were processed by generating maximum-
805 intensity Z-projections, when applicable. The background was subtracted using a
806 rolling ball radius of 30 pixels followed by a Gaussian filter. Pixel intensity values
807 were restricted to a range of 100–350 to exclude background noise and automatic
808 thresholding (default, dark background) was applied. Binary masks were
809 generated and used to quantify area fraction. Logical operations (AND) between
810 processed images were employed to isolate the signal overlap between green
811 and red images; thus, the fusion of photoconverted mitochondria with any
812 mitochondria from the adipocyte network. The fusion process is then measured
813 using the resulting masks. Co-localization was normalized using the ratio of the
814 number of interacting particles to the total number of particles per area.

815 **Time-lapse microscopy analysis**

816 For the time-lapse analysis, we used the methodology described previously [44],
817 with some modifications. In brief, differentiated adipocytes were pretreated for 24
818 h with BSA, palmitate, or BSA before treatment with fluorescent dyes. Mitotracker
819 Green (MTG) was used at 200 nM for 90 minutes and subsequently removed by
820 washing before imaging. Tetramethylrhodamine-ethyl-ester-perchlorate (TMRE)
821 was loaded at 30 nM and remained present during the imaging. The initial
822 photograph was captured at this time point (-1). Subsequently, cells were treated
823 with PAL, BSA, or BSA, initiating a time-lapse sequence for 60 min. Time-lapse
824 images were captured using a Zeiss LSM880 Airyscan microscope with the ZEN
825 Software (Carl Zeiss). The adipocytes were maintained at 37°C in 5% CO2.

826 **Confocal microscopy image processing and analysis**

827 Mitochondrial images were analyzed using Fiji software. The images were
828 smoothed and binarized to analyze the area of single particles. The binary images

829 were then skeletonized, and each skeleton was quantified to obtain the number
830 of networks, junctions, and branches, as well as the length of each particle. Cells
831 exhibiting significant fragmentation of the mitochondrial network were quantified,
832 as previously described [7].

833 **Oil red o staining**

834 After the cells were fixed in 4% PBS-buffered formaldehyde for 30 min, they were
835 washed 3 times and stained with ORO solution (0.3% ORO in 60% isopropanol)
836 for 20 min.

837 **Protein analysis**

838 Cell lysates and tissues were lysed in RIPA buffer (50 mM Tris (Merck), pH 8,
839 150 mM NaCl (Merck), 5 mM EDTA (Merck), 0.1% w/v SDS (Carl Roth), 1% w/v
840 IGEPALCA-630 (Sigma-Aldrich), 0.5% w/v sodium deoxycholate (Sigma-
841 Aldrich)) freshly supplemented with protease inhibitors (Sigma-Aldrich) and
842 phosphatase inhibitors (Roche). The cell lysates were centrifuged for 20 min (4 °C
843 and 13,000 × *g*). Protein concentrations were determined using the Pierce BCA
844 assay (Thermo Fisher Scientific), following the manufacturer's instructions. Equal
845 amounts of solubilized proteins were loaded onto SDS-PAGE gels and blotted
846 onto nitrocellulose or PVDF membranes (Bio-Rad). The membranes were
847 incubated overnight with the primary antibody (E4BP4, 1:1000) in 5% BSA-TBST
848 at 4 °C. After washing with TBST ((200 mM Tris (Merck), 1.36 mM NaCl (Merck),
849 0.1% v/v Tween20 (Sigma-Aldrich)), the membranes were incubated in
850 secondary antibody (Santa Cruz) solutions (1:10,000 in 3% BSA) for 1-2 h at RT
851 and revealed using an enhanced chemiluminescence reagent (Clarity Max
852 Western ECL Substrate, BioRad). Full scans of the uncropped blots are available
853 in Data S2. and incubated overnight with the primary antibodies, as detailed in
854 the reagent table.

855 **AAV injection**

856 Mice were anesthetized with 1-2% isoflurane using a Vaporizer AI-100
857 (Insightltda). A 0.3-0.8 cm longitudinal incision was made in the skin at the
858 interscapular region to expose the brown adipose tissue. Thirty microliters of AAV
859 ($2x10^{11}$ vg/ml) was administered to both lobes of the brown fat depot of mice aged

860 6 weeks using a Hamilton syringe. Following the injections, IPTT-300
861 Temperature Transponders (PLEXX, 11059) were inserted at the midline of the
862 interscapular region. All surgical procedures were performed at least two weeks
863 prior to the initiation of the experiment to allow full recovery.

864 **Animals under cold exposure**

865 Wild-type mice (C57BL6J) were maintained on a 12-h light–dark cycle. For cold
866 exposure, mice were housed at 4°C for 0–14 days. All in vivo experimental
867 procedures in this study were performed during the light phase (07:00–10:00 AM)
868 to avoid significant data variability due to circadian rhythm fluctuations [72].

869 **Indirect calorimetry**

870 Metabolic measurements were obtained using an LE405 Gas Analyzer (Panlab,
871 Harvard Apparatus, Holliston, MA, USA) indirect calorimetry system. Food and
872 water were provided ad libitum to the appropriate devices and were measured
873 using built-in automated instruments. The animals were allowed to acclimatize to
874 the cages for at least 18 h before data acquisition. Data analysis was performed
875 using CalR version 2.0[73].

876 **Brown adipose tissue histology**

877 Dissected BAT samples were fixed in 4% paraformaldehyde, embedded in
878 paraffin, sectioned at 5 mm, and stained with hematoxylin and eosin (H&E). To
879 visualize lipid deposition H&E-stained sections were imaged on a Zeiss Axio
880 Observer microscope (Carl Zeiss). The diameter and area were calculated using
881 ImageJ software. The diameter distribution was estimated for each tissue using
882 weighted kernel density estimation using the Seaborn library[74].

883 **Brown adipose tissue immunohistochemistry**

884 Dissected BAT samples were fixed with 4% paraformaldehyde, embedded in
885 paraffin, and sectioned. First, we employed a method of deparaffinization with
886 100% xylene for 5 min at room temperature, and a second incubation with fresh
887 100% xylene for an additional 5 min to ensure complete removal of paraffin. Next,
888 the slides were rehydrated with 100% ethanol for 5 min and sequentially
889 transferred through a series of ethanol solutions with decreasing concentrations
890 (95%, 90%, 80%, and 70%), and immersed in each solution for 5 min to gradually

891 rehydrate the tissue sections. Finally, the slides were resuspended in PBS. For
892 staining, the same methods as for immunohistochemistry using anti-Tom20 (used
893 for cells) were used without modifications. Images were obtained using a Zeiss
894 LSM880 Airyscan microscope with the ZEN Software (Carl Zeiss).

895 **Brown adipose tissue respiration**

896 Tissue respiration was performed using an O2K high-resolution respirometer
897 (Oroboros Oxygraph-2k; Innsbruck, Austria). Freshly isolated tissues were
898 weighed 2-3 mg and homogenized with BIOPS buffer (2.77 mM of CaK2EGTA,
899 7.23 mM K2EGTA, 0.1 µM free calcium, 20 mM imidazole, 50 mM K+/MES, 0.5
900 mM dithiothreitol, 7 mM MgCl2) and phosphocreatine (15 mM, pH 7.1) at 0-4°C.
901 The homogenized tissue was resuspended in 1 mL MiR05 medium (10 mM
902 KH2PO4, 3 mM MgCl2, 500 µM EGTA, 60 mM lactobionic acid, 20 mM taurine,
903 110 mM sucrose, 1 g/L BSA, and 20 mM HEPES, pH 7.1). Respiratory oxygen
904 flux was assessed at 37°C in MiR05 containing 2 µM digitonin and expressed in
905 picomoles of O2 per second per mg of tissue. L-octanoylcarnitine (1 mM; Sigma),
906 pyruvate (5 mM; Sigma), and malate (2 mM; Sigma), Glutamate (10 mM; Sigma-
907 Aldrich) and succinate (10 mM; Sigma-Aldrich) were added to test complex I and
908 II respiration. Finally, 2 mM GDP (Sigma) was used to estimate the GDP-sensitive
909 respiration.

910 **Glucose and insulin tolerance test**

911 Glucose tolerance tests were performed following the recommendations of [75] in
912 mice after a 6h overnight fast. Glucose was injected intraperitoneal (1.5 g/kg BW),
913 and blood glucose concentrations were measured after 0, 15, 30, 60, 90, and 120
914 min using a glucometer. Insulin tolerance tests were performed after 2h of fasting.
915 After determination of basal blood glucose concentrations, each mouse received
916 an intraperitoneal injection of insulin (0.75 U/kg BW), and blood glucose
917 concentrations were measured using Optium Neo (Abbott, Ireland) after 15, 30,
918 60, 90, 120, and 150 min.

919 **Assessment of mitochondrial morphology via Transmission Electron-**
920 **Microscopy (TEM)**

921 Freshly excised brown adipose tissues were finely minced and subjected to
922 primary fixation in a solution containing 1% glutaraldehyde, 2.5%
923 paraformaldehyde, 100 mM cacodylate buffer (pH 7.4), 6 mM $CaCl_2$, and 4.8%
924 sucrose at 4 °C overnight. Following three washes with 100 mM cacodylate buffer
925 (pH 7.4), samples were immersed in a secondary fixation medium with cacodylate
926 buffer and 2% osmium tetroxide at room temperature for 1 h. After thorough
927 washing, the tissues were pre-stained with saturated uranyl acetate for 50 min at
928 room temperature, dehydrated through a graded acetone series, embedded in
929 Epon epoxy resin, and polymerized at 60 °C for 48 h. Ultrathin sections were
930 examined using a JEM-1400-FLASH Transmission Electron Microscope (JEOL
931 JEM-1400, JEOL, Ltd., Tokyo, Japan). Mitochondrial ultrastructure was analyzed
932 using ImageJ software. The maximum length distribution was estimated for each
933 group using the Seaborn library[74].

934 **Chromatin immunoprecipitation (Chip) assays**

935 Chromatin immunoprecipitation was performed according to the manufacturer's
936 protocol (available at www.abcam.com/protocols/immunoprecipitation-protocol),
937 with some modifications. Briefly, adipocytes were incubated in cross-linking
938 solution (1% formaldehyde) at room temperature for 10 minutes. The cells were
939 then washed twice with 1x PBS and detached from the flask. Subsequently, the
940 cells were resuspended in SDS lysis buffer with protease inhibitors and incubated
941 on ice for 10 min. Chromatin fragmentation was performed by sonication in
942 sodium dodecyl sulfate (SDS) lysis buffer using a Sonic VibraCell. Sonication was
943 performed to obtain DNA fragments with an average size of 150–800 bp.
944 Immunoprecipitation was performed using an anti-E4BP4 antibody (Cell
945 Signaling, mAb #14312). IgG was used as a control. The precipitated DNA was
946 analyzed by qPCR using primers (Table S1) targeting the regulatory region of
947 Cers6 (enhancer).

948 **Site-directed mutagenesis**

949 Site-directed mutagenesis was performed using a Q5 Site-Directed Mutagenesis
950 Kit (NEB) to introduce the desired mutation into the target gene (E4bp4).
951 Mutagenic primers were designed to incorporate mutations at the center of the
952 primers (Table S1). Point mutations were introduced via site-directed

953 mutagenesis to replace asparagine (Asn, AAC) with lysine (Lys, AAG) and
954 glutamic acid (Glu, GAA) with glycine (Gly, GGA), with the aim of evaluating the
955 effects of altered charge and side chain properties on protein function, following
956 a previously published structure analysis [31,32,76]. The reaction mixture included
957 50-100 ng of plasmid DNA (Addgene cat. no 34572) as the template, 0.5 μM of
958 each mutagenic primer (forward and reverse), Q5 hot start and 2X master mix
959 following the manufactures' instructions. After amplification, the reaction was
960 treated with Kinase, Ligase and DpnI (provided in the kit) to digest the parental
961 methylated plasmid DNA, leaving only the newly synthesized, mutated plasmid.
962 The digested plasmid was then transformed into NEB 5-alpha via heat-shock
963 transformation.

964 **LC-MS lipidomic analyses**

965 The lipid extracts stored at -80°C were resuspended in 150 μL of an
966 acetonitrile:isopropanol mixture (70:30 (v:v)) of UPLC grade, followed by
967 agitation. The resuspended samples were centrifuged at 16,000 × g for 5 min,
968 and 100 μL of the supernatant was transferred to 2 mL glass vials. From each
969 analytical sample, a 20 μL aliquot was taken and pooled. These pools were used
970 as quality control samples for instrumental and sample stability (QCs), which
971 were run after every 5th analytical sample in the sample sequence. All the
972 samples and pools were placed in an Acquity iClass UPLC sample manager
973 (Waters) at 4°C. The UPLC system was coupled to a quadrupole time-of-flight
974 (QTOF) system equipped with an ESI source (Xevo G2-XS QTof, Waters). From
975 each lipid sample, 5 μL was injected onto a 100 x 2.1 mm UPLC CSH C18 column
976 packed with 1.7 μm particles (Waters). The UPLC flow rate was set to 200 μL/min,
977 and the buffer system consisted of buffer A (10 mM ammonium formate in
978 acetonitrile:UPLC water (70:30, (v:v))) and buffer B (10 mM ammonium formate
979 in UPLC isopropanol:acetonitrile (90:10, (v:v))). The UPLC gradient was as
980 follows: 0 - 0.80 min 60% A, 0.80-10 min 60 - 0% A, 10-16 min 0% A, 17 min 0 -
981 60% A, 17-22 min re-equilibrating at 60% A. This resulted in a total run time of 22
982 minutes per sample. The mass spectrometer was operated in the negative
983 ionization mode within the mass range of m/z 50-2000. The ESI source was
984 operated with a spray voltage of 2.37 kV in negative ionization mode. Ceramide
985 standard, Cer (16:0) (Avanti Polar Lipids, USA) with a molecular weight of

537.512 g/mol, was used as a reference for retention time and m/z identification under the method's conditions. The ion was identified as the formate adduct (M+HCOO) − with an m/z of 582.51, eluted at a retention time of 9.33 min. An analytical curve for the relative quantification of Cer(d18:1/16:0) in the samples was generated over the concentration range of 12.5 ppm to 50 ppm, with the curve obtained from 3 different concentration points (12.5 ppm, 25 ppm, and 50 ppm), each analyzed in triplicate. The following equation was derived: $y = 1.760 \times - 20.232$, $R^2 = 0.9935$. Relative quantification of ceramide was performed on each sample based on the area under the corresponding ion curve, and an estimate of the concentration of the molecule in the sample was obtained using the calibration curve. The LC-MS data obtained were analyzed using Progenesis QI software (Waters), and untargeted and statistical analyses were conducted using the MetaboAnalyst platform.

Enhancer data analysis

All enhancers related to the regulatory region of Cers6 were downloaded from the database enhanceratlas.org and aligned in the Genome browser UCSC server across different species, including humans and mice. The alignment was generated by the default method using the region established for *the musculus* (65 kb to TSS of Cers6).

ChIP-seq analysis

ChIP-seq data for PRDM16 and PRDM16 knockout (KO) were reanalyzed from a previously published study [53] available at the Gene Expression Omnibus (GSE63965). ChIP-seq data for histone markers (H3K27ac and H3k4Me1) in brown adipose tissue were downloaded from encode project (www.encodeproject.org). ChIP-seq reads were aligned using the Bowtie software [77]. SAM files were then converted into BAM files. Next, peak calling was determined using MACS [78]. Wig to bigWig files were generated, and peaks were visualized using the UCSC Genome Browser. PRDM16 genome-wide binding sites in brown adipose tissue were defined using the Genomic Regions Enrichment of Annotations Tool (GREAT)[79].

RNA preparation and determination of mRNA levels

1017 Total RNA was extracted from cells using TRI reagent (Sigma). CDNA will be
1018 synthesized using High-capacity cDNA Reverse transcription kit (Thermo
1019 Fisher Scientific) according to the provided protocol. qPCR was performed using
1020 Sybr Green (Applied Biosystems) or TaqManTM (Thermo Fisher). The primer
1021 sequences and probes for the target genes are listed in Table S1.

1022 **RNA preparation for RNA-seq**

1023 RNA was extracted from the tissues using the PureLink RNA kit (Invitrogen). A
1024 Bioanalyzer 2100 system (Agilent Technologies) was used to examine RNA
1025 integrity. The sequencing library was built using the Library Prep Kit for Illumina®
1026 and sequencing using the platform NovaSeq PE150.

1027 **Bioinformatics analyses of RNA-seq**

1028 The quality control of the sequences was examined using FastQC (available
1029 online at: http://www.bioinformatics.babraham.ac.uk/projects/fastqc). Clean data
1030 were obtained using Fastp[80] to remove low-quality reads. The data were then
1031 mapped with the *Mus musculus* mm10 genome reference using HISAT2 (v2.1.0)
1032 [81]. The read counts for each gene were calculated using iRNA-seq software.
1033 Differential gene expression was identified by DESeq2 (version 1.10.1). A
1034 heatmap was generated using the pheatmap (R package) to identify differentially
1035 expressed genes. The R package ggplot2 (version 3.3.4) was used to generate
1036 volcano plots. Finally, PathfindR[82] was used for enrichment analysis.

1037 **Bioinformatics analyses of IMAGE**

1038 Data acquisition and preprocessing. RNA-seq and ATAC-seq data were obtained
1039 from NCBI using the public Gene Expression Omnibus database (GSE181443).
1040 The reads obtained were subjected to quality control using the Fast QC tool
1041 (available online at: http://www.bioinformatics.babraham.ac.uk/projects/fastqc).
1042 Low-quality fragments and sequencing adapters were removed using
1043 Trimmomatic. Alignment was performed using the Bowtie2 tool, where the reads
1044 were aligned using the mouse mm10 reference genome. Standardization of the
1045 sequencing data. RNA-seq data aligned against a reference genome were
1046 annotated using iRNA-seq[83]. All data processing was carried out in a Bioconda
1047 environment using the feature counts package as a basis. ATAC-seq data already

aligned against a reference genome were standardized using the Homer package (available at http://biowhat.ucsd.edu/homer) features: makeTagDirectory, findPeaks, mergePeaks, and annotatePeaks). Integration and analysis of the generated data. The files containing RNA-seq and ATAC-seq data were integrated using IMAGE[50] in the Bioconda environment following the recommendations of the author. A file containing the gene expression in RPKM was used for RNA-seq analysis. The files containing information on binding sites for different transcription factors were submitted to GREAT[79] for the annotation of genes related to each site.

Bioinformatics analyses of Single-cell RNA-sequencing (scRNA-seq)

scRNA-seq data available in[84] were re-analyzed using Seurat. Low-quality cells and lowly expressed genes were excluded. Data were normalized using the LogNormalize method and highly variable genes were identified using the VST method. A gene expression matrix was generated for downstream dimensionality reduction, clustering, and differential expression analyses.

Data analysis and graphs

Experiments on the cultured cells were conducted using at least three independent replicates. Comparisons between two independent groups were performed using an unpaired two-tailed Student's t-test. A paired two-tailed Student's t-test was used for comparisons between two groups with matched sample pairs. When comparing datasets with more than two groups, one-way analysis of variance (ANOVA) followed by Tukey's post-hoc multiple comparison test was employed. Statistical analysis for differential expression was performed using a two-sample t-test with Benjamini-Hochberg (BH, FDR of 0.05) correction for multiple testing. The schematic figures were obtained using Biorender. com.

1078 **Table S1:** Primer sequences and probes for qRT-PCR

Mouse qPCR primers

Gene	Forward primer	Reverse primer	Taqman probe
E4bp4	TTCCCCCTCACGGACCAGGGA	CATGGCGTCTTTCTTCTCGTCCGG	
Prdm16	CAGCACGGTGAAGCCATTC	GCGTGCATCCGCTTGTG	
Cers2	TCTTCTCAAAAAGTTCCGAG	AGTGATGATGAAAACGAATGG	
Cers3	CCTGGCTGCTATTAGTCTGATG	CTGCTTCCATCCAGCATAGG	
Cers4	TGTCGTTCAGCTTGAGTGAG	AGCAGGCTTCACAGAATTTC	
Cers5	CTCCAACGCTCACGAAATTTC	ATGCAGACAGAAGATGAGTG	
Sptlc1	TACTCAGAGACCTCCAGCTG	CACCAGGGATATGCTGTCATC	
Sptlc2	GGAGATGCTGAAGCGGAAC	GTATGAGCTGCTGACAGGCA	
Tbp	ACCCTTCACCAATGACTCCTATG	TGACTGCAGCAAATCGCTTGG	
36b4	TCCAGGCTTTGGGCATCA	CTTTATCAGCTGCACATCACTCAGA	
Ucp1	CACCTTCCCGCTGGACACT	CCCTAGGACACCTTTATACCTAATGG	
Tfam	ATTCCGAAGTGTTTTTCCAGCA	TCTGAAAGTTTTGCATCTGGGT	
Nrf1	AGCACGGAGTGACCCAAAC	TGTACGTGGCTACATGGACCT	
Cox8b	TGTGGGGATCTCAGCCATAGT	AGTGGGCTAAGACCCATCCTG	
Cers6	GTTCGGAGCATTCAACGCTG	CTGAGTCGTGAAGACAGAGG	Mm00556165_m1
Rplp0			Mm01974474_gH
Sg1-Enhancer	CACCGGATATGAAAGTCTTTCGAAA	AAACTTTCGAAAGACTTTCATATCC	
Sg2-enhancer	CACCGAAACTATTAAGTAATTCTGC	AAACGCAGAATTACTTAATAGTTTC	
Sg3-enhancer	CACCGCTGTGTGTCACAATTATGAG	AAACCTCATAATTGTGACACACAGC	
Sg4-enhancer	CACCAATTTCAACATTAGGAAAC	AAACGTTTCCTAATGTTGAAATT	
Sg5-enhancer	CACCGCCTTGTAAACATGTCCATT	AATGGACATGTTTACAAGGC	
qPCR-enhancer	GCCACGGTCGAGTCCATGAATG	CTGATTACCAAATACCTTGCC	
Sequencing-enhancer	GGGTACCCAGCAGTGCTAATACC	GGGCTACAGGCACTTTTGACAGC	
Sh-E4bp4	CCGGGCTTCGGACTCCAGGTAAATGCTCGAGCATTTACCTGGAGTCCGAAGCTTTTTG	AATTCAAAAAGCTTCGGACTCCAGGTAAATGCTCGAGCATTTACCTGGAGTCCGAAGC	
Mutagenesis primers	GGAAAAACAAGGGAGCTGCCAAAAG	GCCGTTTCTCCCAATACATG	

Human qPCR primers

Gene	Forward primer	Reverse primer
E4BP4	TCCTCAGTAGAACACACGCAG	TCATCTCTTGGCTCCCTTGT
TBP	CGGCTGTTTAACTTCGCTTCC	TGGGTTATCTTCACACGCCAAG
DIO2	GGAAGAGCTTCCTCCTCGAT	CTGGAGACATGCACCACACT

REFERENCES

1 Cannon, B. & Nedergaard, J. Brown adipose tissue: function and physiological significance. Physiological reviews 84, 277-359, doi:10.1152/physrev.00015.2003 (2004).

2 Chouchani, E. T., Kazak, L. & Spiegelman, B. M. New Advances in Adaptive Thermogenesis: UCP1 and Beyond. Cell metabolism 29, 27-37, doi:10.1016/j.cmet.2018.11.002 (2019).

3 Cohen, P. & Kajimura, S. The cellular and functional complexity of thermogenic fat. Nature reviews. Molecular cell biology 22, 393-409, doi:10.1038/s41580-021-00350-0 (2021).

4 Cypess, A. M. et al. Emerging debates and resolutions in brown adipose tissue research. Cell metabolism 37, 12-33, doi:10.1016/j.cmet.2024.11.002 (2025).

5 Verkerke, A. R. P. et al. BCAA-nitrogen flux in brown fat controls metabolic health independent of thermogenesis. Cell 187, 2359-2374.e2318, doi:10.1016/j.cell.2024.03.030 (2024).

6 Liesa, M. & Shirihai, O. S. Mitochondrial dynamics in the regulation of nutrient utilization and energy expenditure. Cell metabolism 17, 491-506, doi:10.1016/j.cmet.2013.03.002 (2013).

7 Hammerschmidt, P. et al. CerS6-Derived Sphingolipids Interact with Mff and Promote Mitochondrial Fragmentation in Obesity. Cell 177, 1536-1552.e1523, doi:10.1016/j.cell.2019.05.008 (2019).

8 Kelley, D. E., He, J., Menshikova, E. V. & Ritov, V. B. Dysfunction of mitochondria in human skeletal muscle in type 2 diabetes. Diabetes 51, 2944-2950, doi:10.2337/diabetes.51.10.2944 (2002).

9 Xia, W. et al. Obesity causes mitochondrial fragmentation and dysfunction in white adipocytes due to RalA activation. Nature metabolism 6, 273-289, doi:10.1038/s42255-024-00978-0 (2024).

10 Bockus, L. B. et al. Plasma Ceramides and Sphingomyelins and Sudden Cardiac Death in the Cardiovascular Health Study. JAMA network open 6, e2343854, doi:10.1001/jamanetworkopen.2023.43854 (2023).

11 Dagogo-Jack, S. et al. Plasma Ceramides and Other Sphingolipids in Relation to Incident Prediabetes in a Longitudinal Biracial Cohort. The Journal of clinical endocrinology and metabolism 109, 2530-2540, doi:10.1210/clinem/dgae179 (2024).

12 Huynh, K. et al. High-Throughput Plasma Lipidomics: Detailed Mapping of the Associations with Cardiometabolic Risk Factors. Cell chemical biology 26, 71-84.e74, doi:10.1016/j.chembiol.2018.10.008 (2019).

13 Jensen, P. N. et al. Circulating sphingolipids, fasting glucose, and impaired fasting glucose: The Strong Heart Family Study. EBioMedicine 41, 44-49, doi:10.1016/j.ebiom.2018.12.046 (2019).

14 Lemaitre, R. N. et al. Circulating Sphingolipids, Insulin, HOMA-IR, and HOMA-B: The Strong Heart Family Study. Diabetes 67, 1663-1672, doi:10.2337/db17-1449 (2018).

15 Ofori, E. K. et al. Effect of circulating ceramides on adiposity and insulin resistance in patients with type 2 diabetes: An observational cross-sectional study. Endocrinology, diabetes & metabolism 6, e418, doi:10.1002/edm2.418 (2023).

16 Turpin, S. M. et al. Obesity-induced CerS6-dependent C16:0 ceramide production promotes weight gain and glucose intolerance. Cell metabolism 20, 678-686, doi:10.1016/j.cmet.2014.08.002 (2014).

17 Wilkerson, J. L., Tatum, S. M., Holland, W. L. & Summers, S. A. Ceramides are fuel gauges on the drive to cardiometabolic disease. Physiological reviews 104, 1061-1119, doi:10.1152/physrev.00008.2023 (2024).

18 Chaurasia, B. et al. Adipocyte Ceramides Regulate Subcutaneous Adipose Browning, Inflammation, and Metabolism. Cell metabolism 24, 820-834, doi:10.1016/j.cmet.2016.10.002 (2016).
19 Chaurasia, B. et al. Ceramides are necessary and sufficient for diet-induced impairment of thermogenic adipocytes. Molecular metabolism 45, 101145, doi:10.1016/j.molmet.2020.101145 (2021).
20 Gosejacob, D. et al. Ceramide Synthase 5 Is Essential to Maintain C16:0-Ceramide Pools and Contributes to the Development of Diet-induced Obesity. The Journal of biological chemistry 291, 6989-7003, doi:10.1074/jbc.M115.691212 (2016).
21 Holland, W. L. et al. Inhibition of ceramide synthesis ameliorates glucocorticoid-, saturated-fat-, and obesity-induced insulin resistance. Cell metabolism 5, 167-179, doi:10.1016/j.cmet.2007.01.002 (2007).
22 Zhu, Q. et al. PAQR4 regulates adipocyte function and systemic metabolic health by mediating ceramide levels. Nature metabolism 6, 1347-1366, doi:10.1038/s42255-024-01078-9 (2024).
23 Meikle, P. J. & Summers, S. A. Sphingolipids and phospholipids in insulin resistance and related metabolic disorders. Nature reviews. Endocrinology 13, 79-91, doi:10.1038/nrendo.2016.169 (2017).
24 Li, F. et al. Epigenetic interaction between UTX and DNMT1 regulates diet-induced myogenic remodeling in brown fat. Nature communications 12, 6838, doi:10.1038/s41467-021-27141-7 (2021).
25 Zhou, Q. et al. A mouse tissue transcription factor atlas. Nature communications 8, 15089, doi:10.1038/ncomms15089 (2017).
26 Angueira, A. R. et al. Early B Cell Factor Activity Controls Developmental and Adaptive Thermogenic Gene Programming in Adipocytes. Cell reports 30, 2869-2878.e2864, doi:10.1016/j.celrep.2020.02.023 (2020).
27 Hasan, N. et al. Brown adipocyte-specific knockout of Bmal1 causes mild but significant thermogenesis impairment in mice. Molecular metabolism 49, 101202, doi:10.1016/j.molmet.2021.101202 (2021).
28 Kanzleiter, T. et al. Evidence for Nr4a1 as a cold-induced effector of brown fat thermogenesis. Physiological genomics 24, 37-44, doi:10.1152/physiolgenomics.00204.2005 (2005).
29 Plaisier, C. L. et al. Zbtb16 has a role in brown adipocyte bioenergetics. Nutrition & diabetes 2, e46, doi:10.1038/nutd.2012.21 (2012).
30 Cowell, I. G. & Hurst, H. C. Transcriptional repression by the human bZIP factor E4BP4: definition of a minimal repression domain. Nucleic acids research 22, 59-65, doi:10.1093/nar/22.1.59 (1994).
31 Chen, S., Lei, M., Liu, K. & Min, J. Structural basis for specific DNA sequence recognition by the transcription factor NFIL3. The Journal of biological chemistry 300, 105776, doi:10.1016/j.jbc.2024.105776 (2024).
32 Cowell, I. G., Skinner, A. & Hurst, H. C. Transcriptional repression by a novel member of the bZIP family of transcription factors. Molecular and cellular biology 12, 3070-3077, doi:10.1128/mcb.12.7.3070-3077.1992 (1992).
33 Kim, Y. H. & Lazar, M. A. Transcriptional Control of Circadian Rhythms and Metabolism: A Matter of Time and Space. Endocrine reviews 41, 707-732, doi:10.1210/endrev/bnaa014 (2020).

34 Zhao, Z., Yin, L., Wu, F. & Tong, X. Hepatic metabolic regulation by nuclear factor E4BP4. Journal of molecular endocrinology 66, R15-r21, doi:10.1530/jme-20-0239 (2021).
35 Lundgren, P. et al. A subpopulation of lipogenic brown adipocytes drives thermogenic memory. Nature metabolism 5, 1691-1705, doi:10.1038/s42255-023-00893-w (2023).
36 So, J. et al. Chronic cAMP activation induces adipocyte browning through discordant biphasic remodeling of transcriptome and chromatin accessibility. Molecular metabolism 66, 101619, doi:10.1016/j.molmet.2022.101619 (2022).
37 Ganeshan, K. & Chawla, A. Warming the mouse to model human diseases. Nature reviews. Endocrinology 13, 458-465, doi:10.1038/nrendo.2017.48 (2017).
38 Halurkar, M. S. et al. The widely used Ucp1-Cre transgene elicits complex developmental and metabolic phenotypes. Nature communications 16, 770, doi:10.1038/s41467-024-54763-4 (2025).
39 Claflin, K. E. et al. Conditional gene targeting using UCP1-Cre mice directly targets the central nervous system beyond thermogenic adipose tissues. Molecular metabolism 55, 101405, doi:10.1016/j.molmet.2021.101405 (2022).
40 Kim, K. et al. Uncoupling protein 1-driven Cre (Ucp1-Cre) is expressed in the epithelial cells of mammary glands and various non-adipose tissues. Molecular metabolism 84, 101948, doi:10.1016/j.molmet.2024.101948 (2024).
41 Male, V., Nisoli, I., Gascoyne, D. M. & Brady, H. J. E4BP4: an unexpected player in the immune response. Trends in immunology 33, 98-102, doi:10.1016/j.it.2011.10.002 (2012).
42 Da Eira, D., Jani, S. & Ceddia, R. B. An obesogenic diet impairs uncoupled substrate oxidation and promotes whitening of the brown adipose tissue in rats. The Journal of physiology 601, 69-82, doi:10.1113/jp283721 (2023).
43 Schlein, C. et al. Endogenous Fatty Acid Synthesis Drives Brown Adipose Tissue Involution. Cell reports 34, 108624, doi:10.1016/j.celrep.2020.108624 (2021).
44 Wikstrom, J. D. et al. Hormone-induced mitochondrial fission is utilized by brown adipocytes as an amplification pathway for energy expenditure. The EMBO journal 33, 418-436, doi:10.1002/embj.201385014 (2014).
45 Divakaruni, A. S. & Jastroch, M. A practical guide for the analysis, standardization and interpretation of oxygen consumption measurements. Nature metabolism 4, 978-994, doi:10.1038/s42255-022-00619-4 (2022).
46 Summers, S. A., Chaurasia, B. & Holland, W. L. Metabolic Messengers: ceramides. Nature metabolism 1, 1051-1058, doi:10.1038/s42255-019-0134-8 (2019).
47 Raichur, S. et al. CerS2 haploinsufficiency inhibits Î²-oxidation and confers susceptibility to diet-induced steatohepatitis and insulin resistance. Cell metabolism 20, 687-695, doi:10.1016/j.cmet.2014.09.015 (2014).
48 Turpin-Nolan, S. M. & Bruning, J. C. The role of ceramides in metabolic disorders: when size and localization matters. Nature reviews. Endocrinology 16, 224-233, doi:10.1038/s41574-020-0320-5 (2020).
49 Hammerschmidt, P. & Brüning, J. C. Contribution of specific ceramides to obesity-associated metabolic diseases. Cellular and molecular life sciences : CMLS 79, 395, doi:10.1007/s00018-022-04401-3 (2022).
50 Madsen, J. G. S. et al. Integrated analysis of motif activity and gene expression changes of transcription factors. Genome research 28, 243-255, doi:10.1101/gr.227231.117 (2018).

1212 51 Moore, J. E. et al. Expanded encyclopaedias of DNA elements in the human and mouse
1213 genomes. Nature 583, 699-710, doi:10.1038/s41586-020-2493-4 (2020).
1214 52 Hasegawa, Y. et al. Repression of Adipose Tissue Fibrosis through a PRDM16-GTF2IRD1
1215 Complex Improves Systemic Glucose Homeostasis. Cell metabolism 27, 180-194.e186,
1216 doi:10.1016/j.cmet.2017.12.005 (2018).
1217 53 Harms, M. J. et al. PRDM16 binds MED1 and controls chromatin architecture to determine a
1218 brown fat transcriptional program. Genes & development 29, 298-307,
1219 doi:10.1101/gad.252734.114 (2015).
1220 54 Kajimura, S. et al. Regulation of the brown and white fat gene programs through a
1221 PRDM16/CtBP transcriptional complex. Genes & development 22, 1397-1409,
1222 doi:10.1101/gad.1666108 (2008).
1223 55 Kissig, M. et al. PRDM16 represses the type I interferon response in adipocytes to promote
1224 mitochondrial and thermogenic programing. The EMBO journal 36, 1528-1542,
1225 doi:10.15252/embj.201695588 (2017).
1226 56 Valdivieso-Rivera, F. B., de Oliveira Furino, V. & Sponton, C. H. Investigation of Beige Fat
1227 Biology and Metabolism Using the CRISPR SunTag-p65-HSF1 Activation System. Journal of
1228 visualized experiments : JoVE, doi:10.3791/64849 (2023).
1229 57 Cowell, I. G. & Hurst, H. C. Protein-protein interaction between the transcriptional repressor
1230 E4BP4 and the TBP-binding protein Dr1. Nucleic acids research 24, 3607-3613,
1231 doi:10.1093/nar/24.18.3607 (1996).
1232 58 Inagaki, T., Sakai, J. & Kajimura, S. Transcriptional and epigenetic control of brown and beige
1233 adipose cell fate and function. Nature reviews. Molecular cell biology 17, 480-495,
1234 doi:10.1038/nrm.2016.62 (2016).
1235 59 Ohno, H., Shinoda, K., Ohyama, K., Sharp, L. Z. & Kajimura, S. EHMT1 controls brown adipose
1236 cell fate and thermogenesis through the PRDM16 complex. Nature 504, 163-167,
1237 doi:10.1038/nature12652 (2013).
1238 60 Ohno, H., Shinoda, K., Spiegelman, B. M. & Kajimura, S. PPARg agonists induce a white-to-
1239 brown fat conversion through stabilization of PRDM16 protein. Cell metabolism 15, 395-404,
1240 doi:10.1016/j.cmet.2012.01.019 (2012).
1241 61 Wang, Q. et al. Post-translational control of beige fat biogenesis by PRDM16 stabilization.
1242 Nature 609, 151-158, doi:10.1038/s41586-022-05067-4 (2022).
1243 62 Chen, W. J. et al. Characterization of human E4BP4, a phosphorylated bZIP factor. Biochimica
1244 et biophysica acta 1264, 388-396, doi:10.1016/0167-4781(95)00182-4 (1995).
1245 63 Kostrzewski, T. et al. Multiple Levels of Control Determine How E4bp4/Nfil3 Regulates NK Cell
1246 Development. Journal of immunology (Baltimore, Md. : 1950) 200, 1370-1381,
1247 doi:10.4049/jimmunol.1700981 (2018).
1248 64 Zigdon, H. et al. Ablation of ceramide synthase 2 causes chronic oxidative stress due to
1249 disruption of the mitochondrial respiratory chain. The Journal of biological chemistry 288,
1250 4947-4956, doi:10.1074/jbc.M112.402719 (2013).
1251 65 Zhang, S. et al. Sensing ceramides by CYSLTR2 and P2RY6 to aggravate atherosclerosis. Nature,
1252 doi:10.1038/s41586-025-08792-8 (2025).
1253 66 Lin, H. et al. Metabolic signaling of ceramides through the FPR2 receptor inhibits adipocyte
1254 thermogenesis. Science (New York, N.Y.) 388, eado4188, doi:10.1126/science.ado4188
1255 (2025).

67 Becher, T. et al. Brown adipose tissue is associated with cardiometabolic health. Nature medicine 27, 58-65, doi:10.1038/s41591-020-1126-7 (2021).
68 O'Mara, A. E. et al. Chronic mirabegron treatment increases human brown fat, HDL cholesterol, and insulin sensitivity. The Journal of clinical investigation 130, 2209-2219, doi:10.1172/jci131126 (2020).
69 Finlin, B. S. et al. The N23-adrenergic receptor agonist mirabegron improves glucose homeostasis in obese humans. The Journal of clinical investigation 130, 2319-2331, doi:10.1172/jci134892 (2020).
70 Shamsi, F. & Tseng, Y. H. Protocols for Generation of Immortalized Human Brown and White Preadipocyte Cell Lines. Methods in molecular biology (Clifton, N.J.) 1566, 77-85, doi:10.1007/978-1-4939-6820-6_8 (2017).
71 Kluesner, M. G. et al. EditR: A Method to Quantify Base Editing from Sanger Sequencing. The CRISPR journal 1, 239-250, doi:10.1089/crispr.2018.0014 (2018).
72 Deota, S. et al. The time is now: accounting for time-of-day effects to improve reproducibility and translation of metabolism research. Nature metabolism 7, 454-468, doi:10.1038/s42255-025-01237-6 (2025).
73 Mina, A. I. et al. CalR: A Web-Based Analysis Tool for Indirect Calorimetry Experiments. Cell metabolism 28, 656-666.e651, doi:10.1016/j.cmet.2018.06.019 (2018).
74 Waskom, M. L. seaborn: statistical data visualization. Journal of Open Source Software 6, 3021, doi:10.21105/joss.03021 (2021).
75 Virtue, S. & Vidal-Puig, A. GTTs and ITTs in mice: simple tests, complex answers. Nature metabolism 3, 883-886, doi:10.1038/s42255-021-00414-7 (2021).
76 Ikushima, S. et al. Pivotal role for the NFIL3/E4BP4 transcription factor in interleukin 3-mediated survival of pro-B lymphocytes. Proceedings of the National Academy of Sciences of the United States of America 94, 2609-2614, doi:10.1073/pnas.94.6.2609 (1997).
77 Langmead, B., Trapnell, C., Pop, M. & Salzberg, S. L. Ultrafast and memory-efficient alignment of short DNA sequences to the human genome. Genome biology 10, R25, doi:10.1186/gb-2009-10-3-r25 (2009).
78 Zhang, Y. et al. Model-based analysis of ChIP-Seq (MACS). Genome biology 9, R137, doi:10.1186/gb-2008-9-9-r137 (2008).
79 McLean, C. Y. et al. GREAT improves functional interpretation of cis-regulatory regions. Nature biotechnology 28, 495-501, doi:10.1038/nbt.1630 (2010).
80 Chen, S., Zhou, Y., Chen, Y. & Gu, J. fastp: an ultra-fast all-in-one FASTQ preprocessor. Bioinformatics (Oxford, England) 34, i884-i890, doi:10.1093/bioinformatics/bty560 (2018).
81 Kim, D., Langmead, B. & Salzberg, S. L. HISAT: a fast spliced aligner with low memory requirements. Nature methods 12, 357-360, doi:10.1038/nmeth.3317 (2015).
82 Ulgen, E., Ozisik, O. & Sezerman, O. U. pathfindR: An R Package for Comprehensive Identification of Enriched Pathways in Omics Data Through Active Subnetworks. Frontiers in genetics 10, 858, doi:10.3389/fgene.2019.00858 (2019).
83 Madsen, J. G. et al. iRNA-seq: computational method for genome-wide assessment of acute transcriptional regulation from total RNA-seq data. Nucleic acids research 43, e40, doi:10.1093/nar/gku1365 (2015).
84 Song, A. et al. Low- and high-thermogenic brown adipocyte subpopulations coexist in murine adipose tissue. 130, 247-257, doi:10.1172/jci129167 (2020).

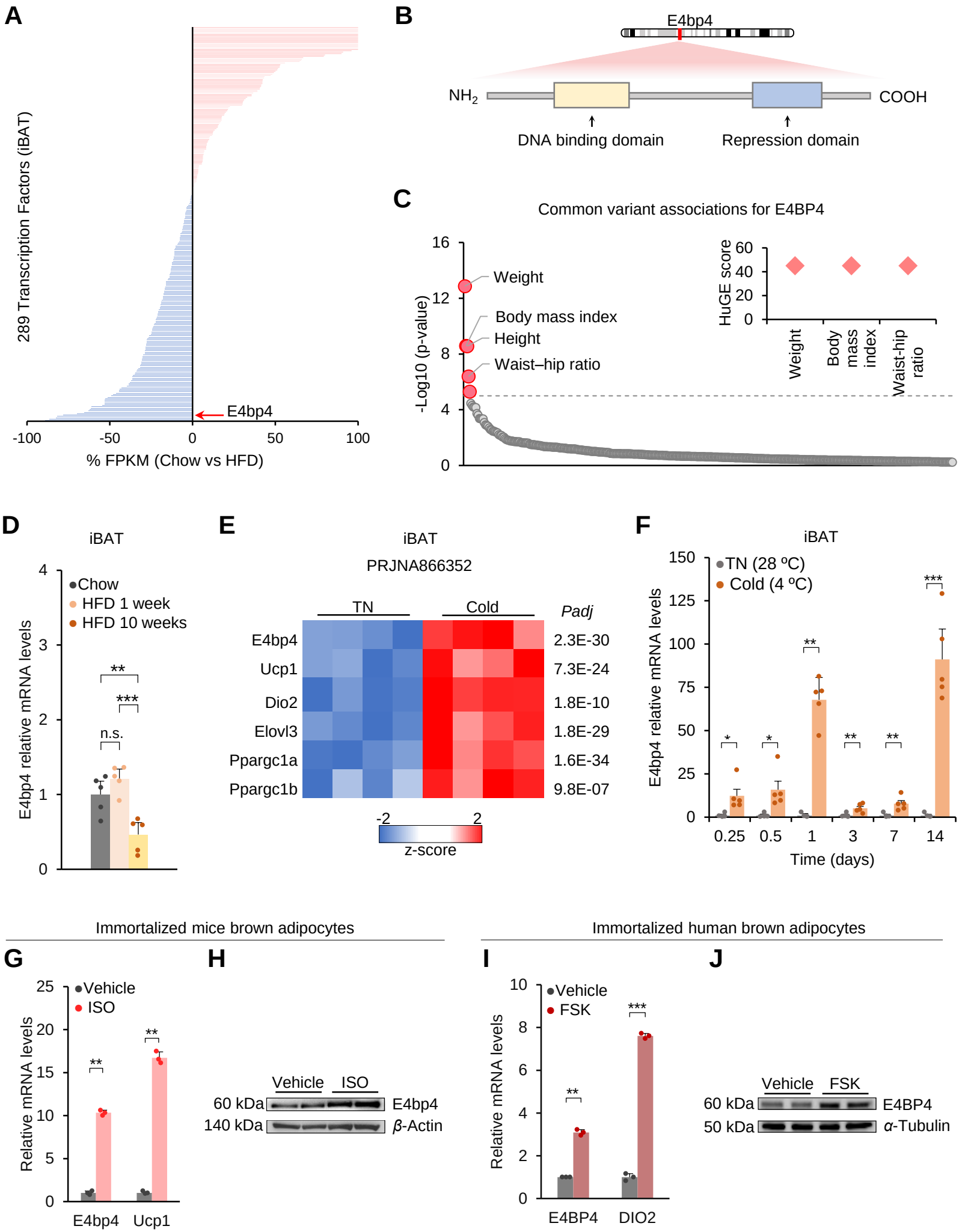
A
289 Transcription Factors (iBAT)
E4bp4
-100
-50
0
50
100
% FPKM (Chow vs HFD)
B
E4bp4
NH2
COOH
DNA binding domain
Repression domain
C
Common variant associations for E4BP4
-Log10 (p-value)
16
12
8
4
0
Weight
Body mass index
Height
Waist–hip ratio
HuGE score
60
40
20
0
Weight
Body mass index
Waist-hip ratio
D
iBAT
E4bp4 relative mRNA levels
Chow
HFD 1 week
HFD 10 weeks
**
***
n.s.
E
iBAT
PRJNA866352
TN
Cold
Padj
E4bp4
Ucp1
Dio2
Elovl3
Ppargc1a
Ppargc1b
2.3E-30
7.3E-24
1.8E-10
1.8E-29
1.6E-34
9.8E-07
-2
2
z-score
F
iBAT
E4bp4 relative mRNA levels
TN (28 ºC)
Cold (4 ºC)
*
*
**
**
**
***
0.25
0.5
1
3
7
14
Time (days)
Immortalized mice brown adipocytes
G
Relative mRNA levels
Vehicle
ISO
**
**
E4bp4
Ucp1
H
Vehicle
ISO
60 kDa
E4bp4
140 kDa
β-Actin
Immortalized human brown adipocytes
I
Relative mRNA levels
Vehicle
FSK
**
***
E4BP4
DIO2
J
Vehicle
FSK
60 kDa
E4BP4
50 kDa
α-Tubulin

Figure 1. E4bp4 is a DNA-binding TF repressed by diet-induced obesity (DIO) and stimulated by cold and adrenergic signaling

A. FPKM-based quantification of expression changes (percentage) of 289 transcription factors in interscapular brown adipose tissue (iBAT) from mice fed a high-fat diet (HFD) versus a chow diet. Data are available in the Gene Expression Omnibus under the accession code GSE175608.

B. Schematic representation of the transcription factor E4bp4. The basic leucine zipper (bZIP) domain and minimal repressor domain are indicated, illustrating regions critical for DNA binding and transcriptional repression.

C. Left: The region page near the E4BP4 gene shows significant associations (above dash line) generated by bottom-line meta-analysis across all datasets in the Common Metabolic Diseases Knowledge Portal (CMDKP). Right: scores from the Human Genetic Evidence (HuGE) calculator on the gene page.

D. Relative mRNA levels of E4pb4 in iBAT from HFD (1 and 10 weeks) and chow diet (10 weeks) control mice. n = 5 per group.

E. *Heat map* of RNA-seq transcriptome of iBAT in animals under cold or thermoneutral (TN) stress. n = 4 per group. Data are represented as Z scores. Data are available from the BioProject: PRJNA866352.

F. Relative mRNA levels of E4pb4 in iBAT from animals exposed to cold stress and thermoneutrality. n = 5 per group.

G. Relative mRNA levels of E4pb4 and Ucp1 in brown adipocytes treated with isoproterenol (1 μM) or vehicle for 24 h. n = 3 per group.

H. Western blotting for E4bp4 in brown adipocytes treated with isoproterenol (1 μM) or vehicle for 24 h. Representative results are shown from two independent experiments. Gel source data are presented in the Supplementary data.

I. Relative mRNA levels of E4BP4 and DIO2 in immortalized human brown adipocytes treated with forskolin (20 μM) or vehicle for 24 h. n = 3 per group.

J. Western blotting for E4BP4 in immortalized human brown adipocytes treated with forskolin (20 μM) or vehicle for 24 h. Representative results are shown from two independent experiments. Gel source data are presented in the Supplementary data.

For D, F, G, and I, data are presented as the mean±SEM. Two-sided P values were calculated using unpaired Student's t-tests (E, F, G, and I). Two-way ANOVA with Tukey's multiple comparison test (D). *P < 0.05, **P < 0.01, ***P < 0.001.

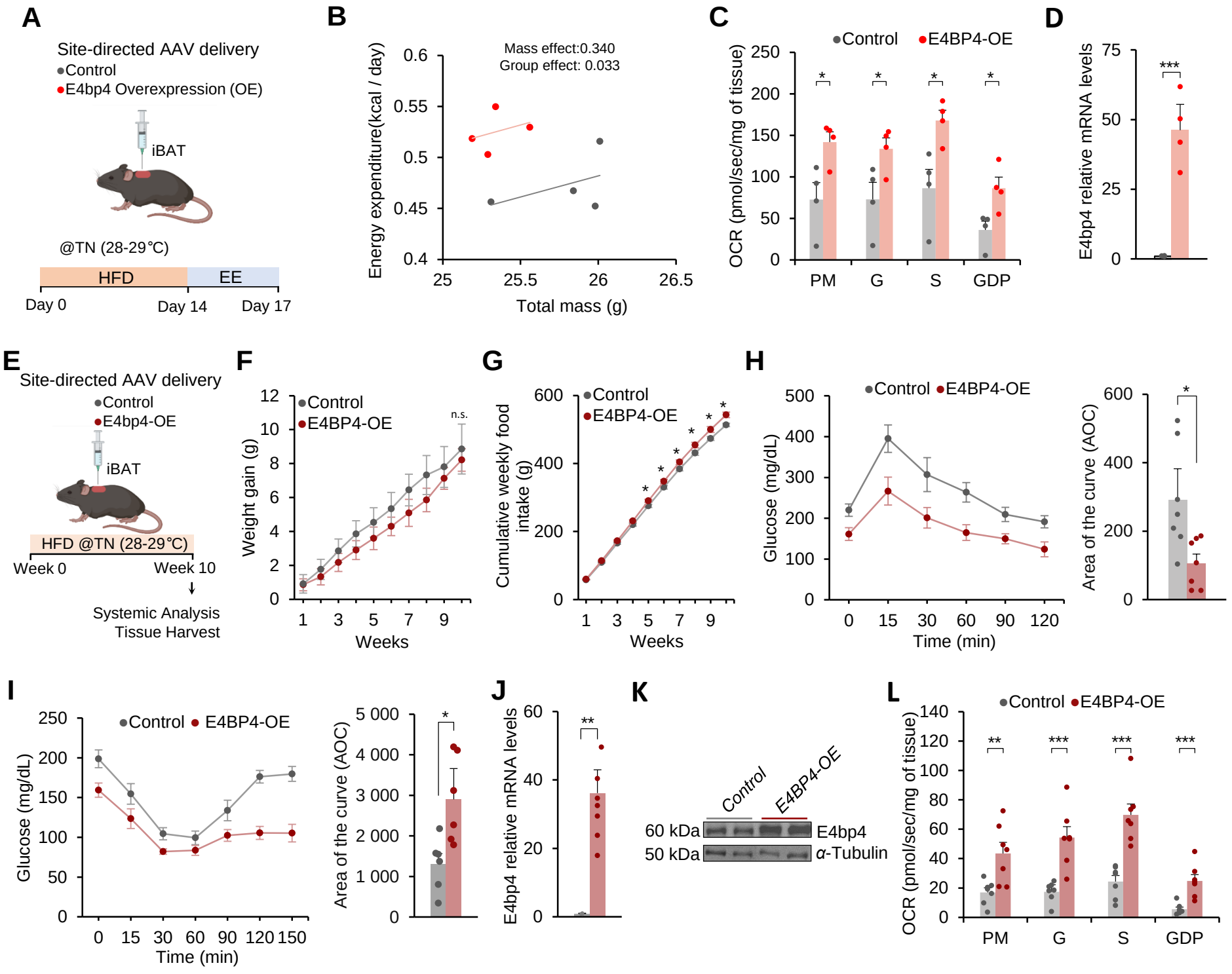
A
Site-directed AAV delivery
Control
E4bp4 Overexpression (OE)
iBAT
@TN (28-29°C)
HFD
EE
Day 0
Day 14
Day 17
B
Mass effect:0.340
Group effect: 0.033
Energy expenditure(kcal / day)
Total mass (g)
C
Control
E4BP4-OE
OCR (pmol/sec/mg of tissue)
PM
G
S
GDP
D
E4bp4 relative mRNA levels
E
Site-directed AAV delivery
Control
E4bp4-OE
iBAT
HFD @TN (28-29°C)
Week 0
Week 10
Systemic Analysis
Tissue Harvest
F
Weight gain (g)
Weeks
n.s.
G
Cumulative weekly food intake (g)
H
Glucose (mg/dL)
Time (min)
Area of the curve (AOC)
I
Glucose (mg/dL)
Time (min)
Area of the curve (AOC)
J
E4bp4 relative mRNA levels
K
Control
E4BP4-OE
60 kDa
50 kDa
E4bp4
α-Tubulin
L
OCR (pmol/sec/mg of tissue)

Figure 2. E4bp4 prevents obesity-induced impairment of systemic energy homeostasis

A. Schematic illustration of experimental design (A-D) for overexpression of E4bp4 (E4BP4-OE) or control in iBAT. The cartoon was created using a Biorender.

B. Regression-based analysis of energy expenditure (EE) against body mass. Data were analyzed using a CaIR2-ANCOVA with EE as a dependent variable and body mass as a covariate. n = 4 per group.

C. Mitochondrial oxygen consumption of iBAT in the presence of pyruvate/malate (PM), glutamate (G), succinate (S), and GDP-sensitive (UCP1 inhibitor). n = 4 per group.

D. Relative mRNA levels of E4pb4 in iBAT from Control and E4BP4-OE after 2 weeks of HFD. n = 4 per group.

E. Schematic illustration of the experimental design for overexpression of E4bp4 (E4BP4-OE) or Control in IBAT (F-L). The cartoon was created using a Biorender.

F. Weight gain of Control and E4BP4-OE mice fed a HFD at 28-29°C. n = 7 per group.

G. Cumulative weekly food intake of Control and E4BP4-OE mice fed a HFD at 28-29°C. n = 7 per group.

H. Left: Glucose tolerance test of mice after 10 weeks of HFD. Right: Area of curve. n = 7 per group.

I. Left: Insulin-tolerance test of mice after 10 weeks of HFD feeding. Right: Area of curve. n = 7 per group.

J. Relative mRNA levels of E4pb4 in iBAT of Control and E4BP4-OE mice fed a HFD at 28-29°C. n = 7 per group.

K. Western blotting for E4bp4 in iBAT of Control and E4BP4-OE mice fed an HFD at 28-29°C. Representative results are shown from two independent experiments. Gel source data are presented in the Supplementary data.

L. Mitochondrial oxygen consumption of iBAT in the presence of pyruvate/malate (PM), glutamate (G), succinate (S), and GDP-sensitive (UCP1 inhibitor). n = 7 per group.

For C, D, F, G, H, I, J, and L, data are presented as the mean±SEM. Two-sided P values were calculated using unpaired Student's t-tests (C, D, H-L). Two-way ANOVA with Tukey's multiple comparison test (F, G). *P < 0.05, **P < 0.01, ***P < 0.001.

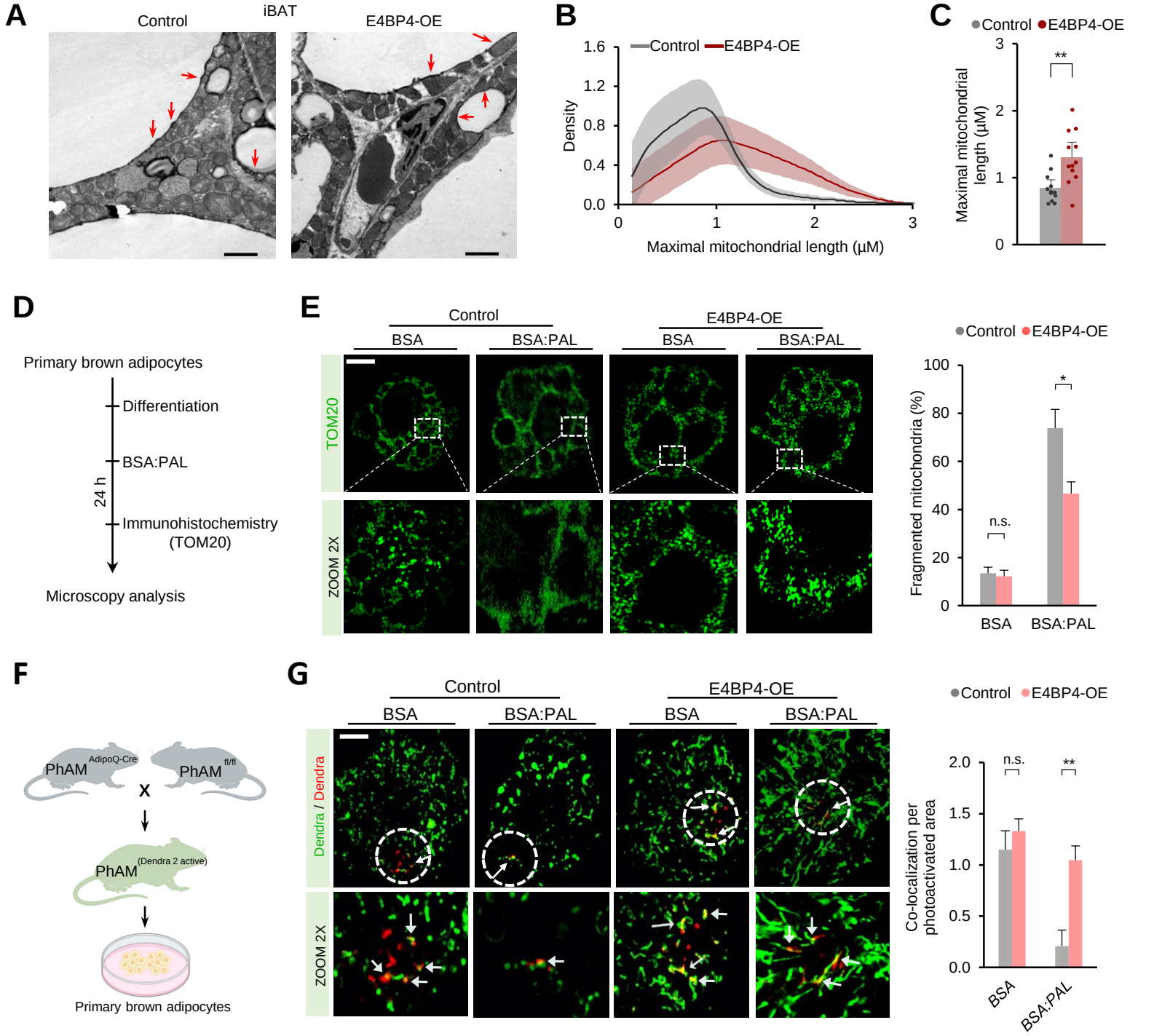
A
iBAT
Control
E4BP4-OE
B
Control
E4BP4-OE
Density
Maximal mitochondrial length (µM)
C
Control
E4BP4-OE
Maximal mitochondrial length (µM)
**
D
Primary brown adipocytes
Differentiation
BSA:PAL
24 h
Immunohistochemistry (TOM20)
Microscopy analysis
E
Control
E4BP4-OE
BSA
BSA:PAL
TOM20
ZOOM 2X
Fragmented mitochondria (%)
n.s.
*
F
PhAM AdipoQ-Cre
PhAM fl/fl
x
PhAM (Dendra 2 active)
Primary brown adipocytes
G
Dendra / Dendra
ZOOM 2X
Co-localization per photoactivated area
n.s.
**
H
Pre-treatment PAL or BSA 24 h
TMRE/MTG
TMRE/MTG image
PAL or BSA Start time lapse
0 min
washout
90 min
92 min (-1)
95 min
Time (min): -1 2 5 7 60
BSA
BSA:PAL
Control
E4bp4-OE
TMRE/MTG relative to time-1
Time (min)
I
Control (PA_6H)
Control (PA_24H)
E4BP4-OE (PA_6H)
E4BP4-OE (PA_24H)
NE
Oligo
FCCP
Rot/AA
OCR (pmol/min/µg protein)
Time (min)

Figure 3. E4BP4 prevents obesity-induced mitochondria fragmentation

A. Transmission electron microscopy (TEM) of mitochondrial morphology in iBAT at 28-29°C in control and E4BP4-OE mice after 10 weeks of HFD feeding. Representative image. Scale bar: 2 μm.

B. Histogram of maximal mitochondrial length of A.

C. Quantification of maximal mitochondrial length (n = 3 per group).

D. Schematic illustration of experimental design for E. The cartoon was created using a Biorender.

E. Right: Images of mitochondrial morphology in primary brown adipocytes by TOM20 immunocytochemistry after 24 h of control treatment (BSA) or palmitate stimulation (BSA:PAL). Representative image. Scale bar, 10 μm. Left: Quantification of cells with a fragmented mitochondrial network (n = 3; 100-220 mitochondria from 10 images/group/experiment).

F. Breeding strategy for PhAM$^{(\text{Dendra2 active})}$ mice and littermate control mice. Primary brown adipocytes were used in the experiments. The cartoon was created using a Biorender.

G. Left: live-cell fluorescence of MitoDendra2 in primary brown adipocytes infected with AAV-control or E4BP4. Arrows show the colocalization of the active Dendra. Representative image. Scale bar, 12 μm. Right: Quantification of colocalization of Dendra active and not-activated.

H. Top: Schematic illustration of the experimental design. Bottom left: Wave-like mitochondrial depolarization in primary brown adipocytes infected with AAV-Control and E4bp4 stained with TMRE (red) and MTG (green) stimulated with palmitate. Time-lapse imaging was performed at the onset of mitochondrial depolarization. Scale bar 5 μm. Bottom right: Quantification of depolarization occurring pre- and post-mitochondrial fragmentation (relative to minute -1).

I. OCR in differentiated primary brown adipocytes expressing Control or E4bp4 after pretreatment for 6 or 24 h with control treatment (BSA) or palmitate stimulation (BSA:PAL). OCR values were normalized to total protein (μg). n = 5 per group. Norepinephrine (NE), oligomycin (oligo), carbonyl cyanide-p-trifluoromethoxyphenylhydrazone (FCCP), rotenone, and antimycin A (Rot/AA).

For B, C, E, G, H, and I, data are presented as mean±SEM. Two-sided P-values were calculated using unpaired Student's t-tests (C and H). Two-way ANOVA with Tukey's multiple comparison test (E, G, and I). *P < 0.05, **P < 0.01, ***P < 0.001.

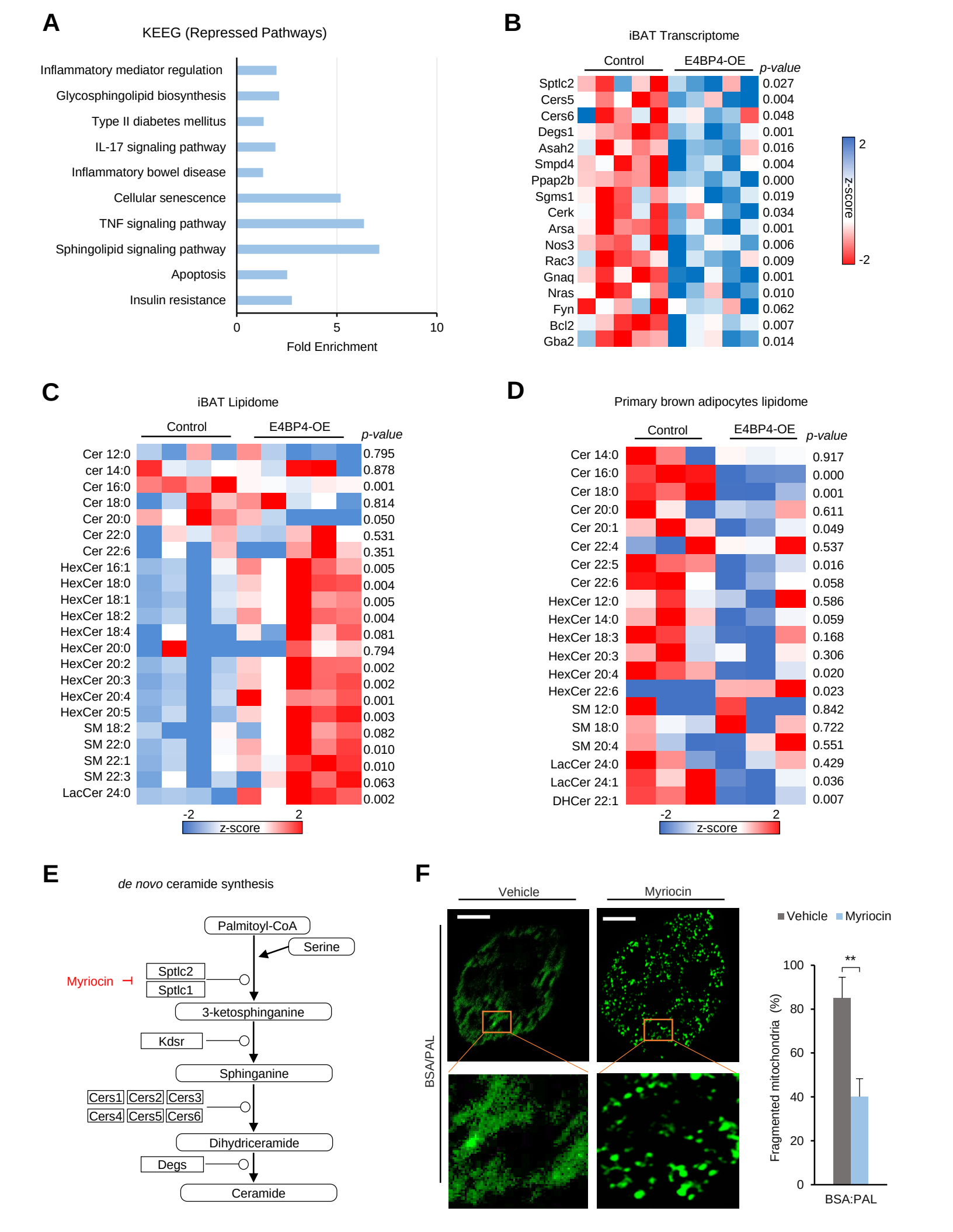
A
KEEG (Repressed Pathways)
Inflammatory mediator regulation
Glycosphingolipid biosynthesis
Type II diabetes mellitus
IL-17 signaling pathway
Inflammatory bowel disease
Cellular senescence
TNF signaling pathway
Sphingolipid signaling pathway
Apoptosis
Insulin resistance
0
5
10
Fold Enrichment
B
iBAT Transcriptome
Control
E4BP4-OE
p-value
Sptlc2 0.027
Cers5 0.004
Cers6 0.048
Degs1 0.001
Asah2 0.016
Smpd4 0.004
Ppap2b 0.000
Sgms1 0.019
Cerk 0.034
Arsa 0.001
Nos3 0.006
Rac3 0.009
Gnaq 0.001
Nras 0.010
Fyn 0.062
Bcl2 0.007
Gba2 0.014
2
z-score
-2
C
iBAT Lipidome
Control
E4BP4-OE
p-value
Cer 12:0 0.795
cer 14:0 0.878
Cer 16:0 0.001
Cer 18:0 0.814
Cer 20:0 0.050
Cer 22:0 0.531
Cer 22:6 0.351
HexCer 16:1 0.005
HexCer 18:0 0.004
HexCer 18:1 0.005
HexCer 18:2 0.004
HexCer 18:4 0.081
HexCer 20:0 0.794
HexCer 20:2 0.002
HexCer 20:3 0.002
HexCer 20:4 0.001
HexCer 20:5 0.003
SM 18:2 0.082
SM 22:0 0.010
SM 22:1 0.010
SM 22:3 0.063
LacCer 24:0 0.002
-2
2
z-score
D
Primary brown adipocytes lipidome
Control
E4BP4-OE
p-value
Cer 14:0 0.917
Cer 16:0 0.000
Cer 18:0 0.001
Cer 20:0 0.611
Cer 20:1 0.049
Cer 22:4 0.537
Cer 22:5 0.016
Cer 22:6 0.058
HexCer 12:0 0.586
HexCer 14:0 0.059
HexCer 18:3 0.168
HexCer 20:3 0.306
HexCer 20:4 0.020
HexCer 22:6 0.023
SM 12:0 0.842
SM 18:0 0.722
SM 20:4 0.551
LacCer 24:0 0.429
LacCer 24:1 0.036
DHCer 22:1 0.007
-2
2
z-score
E
de novo ceramide synthesis
Palmitoyl-CoA
Serine
Myriocin
Sptlc2
Sptlc1
3-ketosphinganine
Kdsr
Sphinganine
Cers1 Cers2 Cers3
Cers4 Cers5 Cers6
Dihydriceramide
Degs
Ceramide
F
Vehicle
Myriocin
BSA/PAL
Vehicle
Myriocin
**
100
80
60
40
20
0
Fragmented mitochondria (%)
BSA:PAL

Figure 4. E4BP4 suppresses lipid overload-induced mitochondria fragmentation by repressing ceramide synthesis

A. Gene ontology analysis of repressed KEGG pathways in iBAT from E4BP4-OE versus control mice after 10 weeks of HFD at thermoneutrality (28–29°C). The data are presented as fold-enrichment.

B. Heat map of selected genes from the sphingolipid signaling pathway based on RNA-seq analysis of iBAT from E4BP4-OE and control mice (n = 5 per group). Data are represented as Z scores.

C. Heat map of iBAT lipidome of control (n=4) and E4BP4-OE (n = 5). Data are represented as Z scores.

D. Heatmap showing whole-cell lipidome of Control and E4BP4-OE primary brown adipocytes. Data are represented as Z scores.

E. Schematic of de novo ceramide synthesis.

F. Left: Images of mitochondrial morphology in primary brown adipocytes by TOM20 immunocytochemistry after 24 h of control treatment (BSA) or palmitate stimulation (BSA:PAL). Representative image. Scale bar, 12 μm. Right: Quantification of cells with a fragmented mitochondrial network (n = 3; 100-180 mitochondria from five images/group/experiment).

For F data is presented as mean±SEM. Two-sided P-values were calculated using unpaired Student's t-tests (B-D–D and F). *P < 0.05, **P < 0.01, ***P < 0.001.

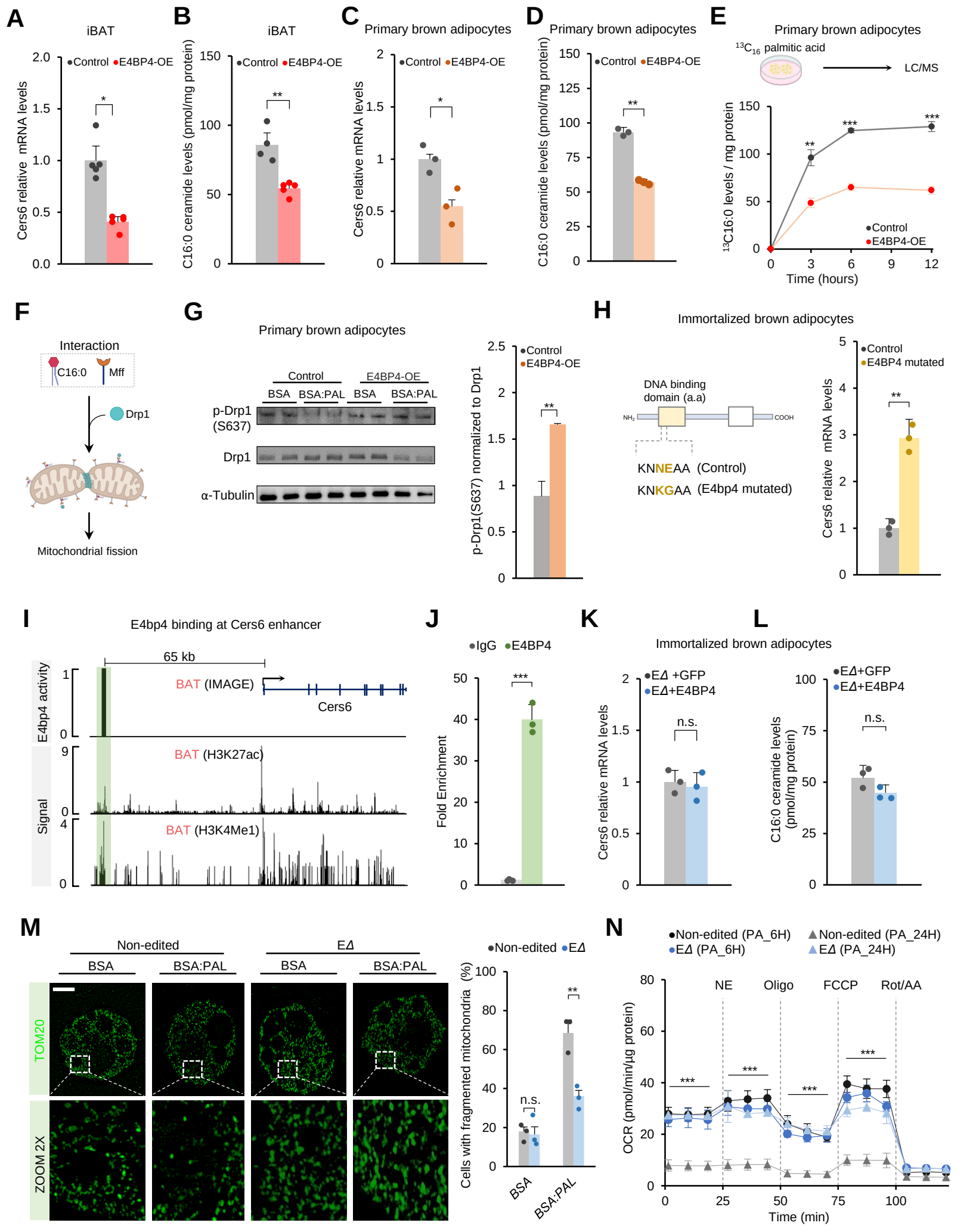
A
iBAT
Control
E4BP4-OE
Cers6 relative mRNA levels
B
iBAT
C16:0 ceramide levels (pmol/mg protein)
C
Primary brown adipocytes
Cers6 relative mRNA levels
D
Primary brown adipocytes
C16:0 ceramide levels (pmol/mg protein)
E
Primary brown adipocytes
13C16 palmitic acid
LC/MS
13C16:0 levels / mg protein
Time (hours)
F
Interaction
C16:0
Mff
Drp1
Mitochondrial fission
G
Primary brown adipocytes
Control
E4BP4-OE
BSA
BSA:PAL
p-Drp1 (S637)
Drp1
α-Tubulin
p-Drp1(S637) normalized to Drp1
H
Immortalized brown adipocytes
DNA binding domain (a.a)
NH2
COOH
KNNEAA (Control)
KNKGAA (E4bp4 mutated)
E4BP4 mutated
Cers6 relative mRNA levels
I
E4bp4 binding at Cers6 enhancer
65 kb
E4bp4 activity
BAT (IMAGE)
Cers6
Signal
BAT (H3K27ac)
BAT (H3K4Me1)
J
IgG
E4BP4
Fold Enrichment
K
Immortalized brown adipocytes
EΔ +GFP
EΔ+E4BP4
n.s.
Cers6 relative mRNA levels
L
C16:0 ceramide levels (pmol/mg protein)
M
Non-edited
EΔ
BSA
BSA:PAL
TOM20
ZOOM 2X
Cells with fragmented mitochondria (%)
N
Non-edited (PA_6H)
EΔ (PA_6H)
Non-edited (PA_24H)
EΔ (PA_24H)
NE
Oligo
FCCP
Rot/AA
OCR (pmol/min/µg protein)
Time (min)

Figure 5. E4BP4 suppresses mitochondrial fragmentation through inhibition of Cers6-driven C16 ceramide synthesis

A. Relative mRNA levels of Cers6 in iBAT of Control and E4BP4-OE mice fed a HFD at 28-29°C. n = 5 per group.

B. C16:0 levels in iBAT of Control and E4BP4-OE mice fed a HFD at 28-29°C. n = 5 per group.

C. Relative mRNA levels of Cers6 in primary brown adipocytes of the Control and E4BP4-OE groups. n = 3 per group.

D. C16:0 quantification by mass spectrometry in primary brown adipocytes of the Control and E4BP4-OE groups. C16:0 levels were normalized to total protein (μg). n = 3 per group.

E. C16:0 quantification by mass spectrometry in primary brown adipocytes of Control and E4BP4-OE treated for 3, 6, and 12 h with $^{13}C_{16}$ palmitic acid. C16:0 levels were normalized to total protein (μg). n = 3 per group.

F. A schematic of the mechanism of action of C16:0 binding to the mitochondrial fission factor (Mff), which is a dynamin-related protein-1 (Drp1) adaptor that induces mitochondrial fragmentation.

G. Left: Immunoblotting of phospho-Drp1 (S637) and total Drp1 in primary brown adipocytes of Control and E4BP4-OE after 24 h of control treatment (BSA) or palmitate stimulation (BSA:PAL). Representative results are shown from two independent experiments. Gel source data are presented in the Supplementary data. Right: quantification of phospho-Drp1 (S637).

H. Left: Schematic of the mutagenesis site directed on the DNA-binding domain or E4bp4. Right: Relative mRNA levels of Cers6 in brown adipocytes from Control and E4BP4-mutated cells. n = 3 per group.

I. Top: Peak of E4bp4 activity results from IMAGE analysis in BAT. Bottom: H3K27ac and H3K4me1 signals at *Cers6* loci in BAT.

J. Fold enrichment at the binding motif site of E4bp4 (I) in brown adipocytes. The enrichment was assessed by qPCR compared to IgG control. n=3.

K. Relative mRNA levels of Cers6 of brown adipocytes mutant E0697815 (ΔE) overexpressing GFP or E4bp4. n=3.

L. C16:0 quantification by mass spectrometry of brown adipocytes mutant E0697815 (ΔE) overexpressing GFP or E4bp4. n=3.

M. Left: images of mitochondrial morphology in brown adipocytes mutant E0697815 (ΔE) or control (Non-edited) by TOM20 immunocytochemistry after 24 hours of control treatment (BSA) or palmitate stimulation (BSA:PAL). Representative image. Scale bar, 10 μm. Right: quantification of cells with a fragmented mitochondrial network. n = 3.

N. The OCR in differentiated brown adipocytes mutant E0697815 (ΔE) or control (Non-edited) after a pre-treatment of 6 or 24 hours with control treatment (BSA) or palmitate stimulation (BSA:PAL). OCR values were normalized by total protein (μg). n = 5 per group. Norepinephrine (NE), oligomycin (oligo), carbonyl cyanide-p-trifluoromethoxyphenylhydrazone (FCCP), and rotenone and antimycin A (Rot/AA).

For A-E, G, H, and J-N data are mean ± SEM. Two-sided P values were calculated using unpaired Student's t-tests (A, B, C, D, E, G, H, J, K, and L). Two-way ANOVA with Tukey's multiple comparisons test (M and N). *P < 0.05, **P < 0.01, ***P < 0.001.

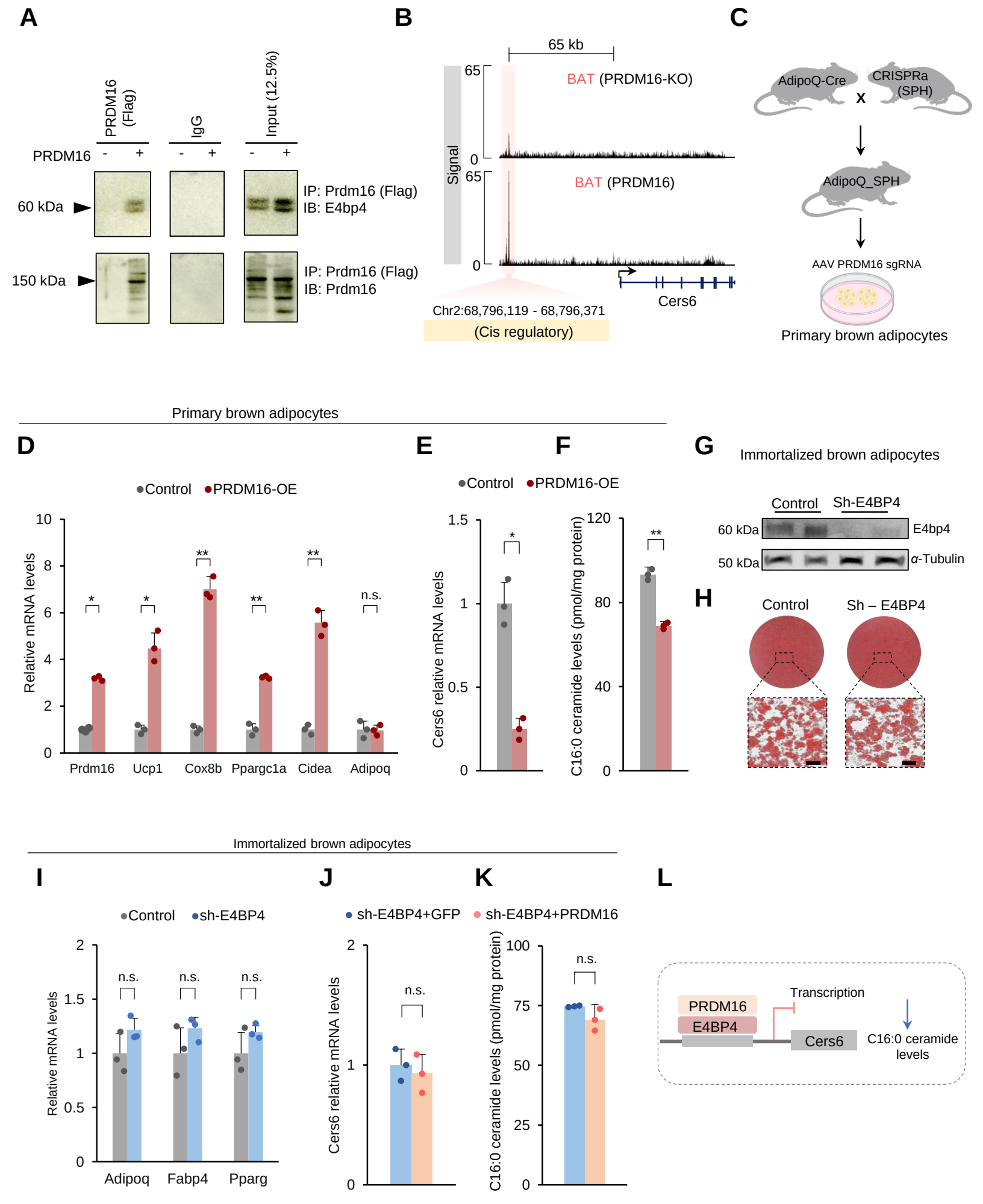
A
PRDM16 (Flag)
IgG
Input (12.5%)
PRDM16
60 kDa
150 kDa
IP: Prdm16 (Flag)
IB: E4bp4
IP: Prdm16 (Flag)
IB: Prdm16
B
65 kb
BAT (PRDM16-KO)
BAT (PRDM16)
Signal
Chr2:68,796,119 - 68,796,371
(Cis regulatory)
Cers6
C
AdipoQ-Cre
CRISPRa (SPH)
AdipoQ_SPH
AAV PRDM16 sgRNA
Primary brown adipocytes
Primary brown adipocytes
D
Control
PRDM16-OE
Relative mRNA levels
Prdm16
Ucp1
Cox8b
Ppargc1a
Cidea
Adipoq
n.s.
E
Cers6 relative mRNA levels
F
C16:0 ceramide levels (pmol/mg protein)
G
Immortalized brown adipocytes
Control
Sh-E4BP4
60 kDa
50 kDa
E4bp4
α-Tubulin
H
Control
Sh – E4BP4
Immortalized brown adipocytes
I
Control
sh-E4BP4
Relative mRNA levels
Adipoq
Fabp4
Pparg
J
sh-E4BP4+GFP
sh-E4BP4+PRDM16
Cers6 relative mRNA levels
K
C16:0 ceramide levels (pmol/mg protein)
L
PRDM16
E4BP4
Transcription
Cers6
C16:0 ceramide levels

Figure 6. E4BP4 interacts with PRDM16 to inhibit Cers6-driven C16 ceramide synthesis

A. PRDM16 complex was immunopurified from differentiated brown adipocytes. Endogenous E4bp4 was detected by immunoblotting.

B. ChIP-seq for PRDM16 and PRDM16 knockout (PRDM16-KO) on the Cers6 gene in BAT.

C. Breeding strategy for AdipoQ_SPH mice and littermate control mice. Primary brown adipocytes were used in the experiments. The cartoon was created using a Biorender.

D. Relative mRNA levels of indicate genes in primary brown adipocytes of the Control and PRDM16-OE groups. n = 3 per group.

E. Relative mRNA levels of Cers6 in primary brown adipocytes of the Control and PRDM16-OE groups. n = 3 per group.

F. C16:0 quantification by mass spectrometry in primary brown adipocytes of the Control and PRDM16-OE groups. C16:0 levels were normalized to total protein (μg). n = 3 per group.

G. Western blotting for E4bp4 in immortalized brown adipocytes with knockdown for E4bpa (sh-E4BP4) or control. Representative results are shown from two independent experiments. Gel source data are presented in the Supplementary data.

H. Representative images of Oil Red O staining in control and sh-E4BP4 brown adipocytes after seven days of differentiation.

I. Relative mRNA levels of adipogenic genes in immortalized brown adipocytes of the Control and sh-E4BP4. n = 3 per group.

J. Relative mRNA levels of Cers6 of brown adipocytes sh-E4BP4 overexpressing GFP or Prdm16. n=3.

K. C16:0 quantification by mass spectrometry of brown adipocytes sh-E4BP4 overexpressing GFP or Prdm16. n=3.

L. A proposed mechanism by which E4BP4-PRDM16 complex controls Cers6 expression.

For D-F, and I-K data are presented as mean±SEM. Two-sided P-values were calculated using an unpaired Student's t-test (D, E, F, I, J, and K). *P < 0.05, **P < 0.01, ***P < 0.001.

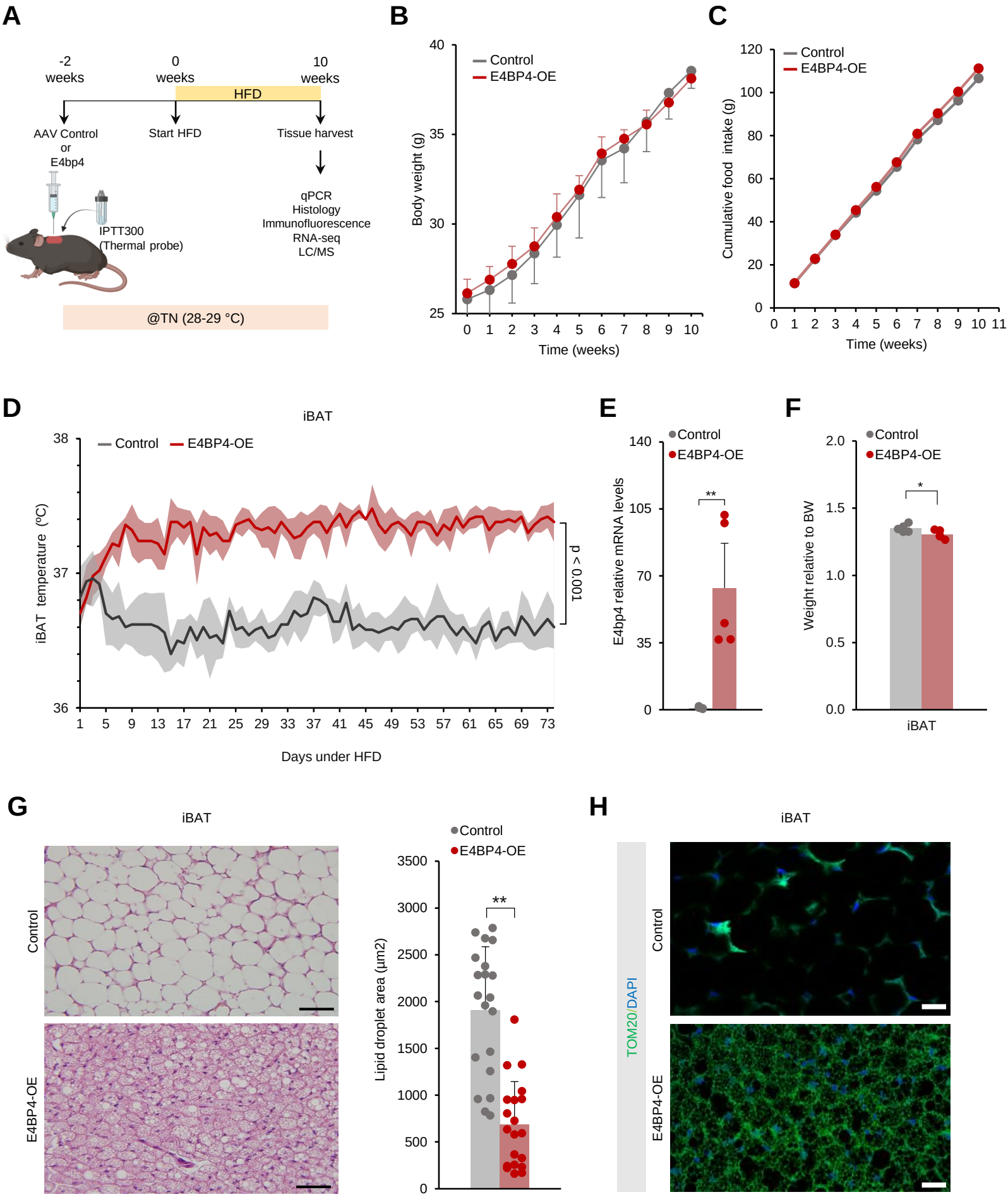
A
-2 weeks
0 weeks
10 weeks
HFD
AAV Control or E4bp4
Start HFD
Tissue harvest
qPCR
Histology
Immunofluorescence
RNA-seq
LC/MS
IPTT300 (Thermal probe)
@TN (28-29 °C)
B
Control
E4BP4-OE
Body weight (g)
Time (weeks)
C
Control
E4BP4-OE
Cumulative food intake (g)
Time (weeks)
D
iBAT
Control
E4BP4-OE
iBAT temperature (°C)
p < 0.001
Days under HFD
E
Control
E4BP4-OE
E4bp4 relative mRNA levels
**
F
Control
E4BP4-OE
Weight relative to BW
*
iBAT
G
iBAT
Control
E4BP4-OE
Lipid droplet area (µm2)
**
H
iBAT
TOM20/DAPI
Control
E4BP4-OE

Figure S1. Analysis of E4BP4-OE in DIO mice using AAV constitutive CMV promoter (Related to figure 2)

A. Schematic illustration of experimental design (A-H) for overexpression of E4bp4 (E4BP4-OE) or control in iBAT. The cartoon was created using a Biorender.
B. Body-weight of Control or E4BP4-OE mice under HFD at 28-29 °C. n = 5 per group.
C. Cummulative food intake of Control or E4BP4-OE mice under HFD at 28-29 °C. n = 5 per group.
D. Temperature of iBAT of Control or E4BP4-OE mice under HFD at 28-29 °C. n = 5 per group.
E. Relative mRNA levels of E4pb4 in iBAT of Control and E4BP4-OE mice fed a HFD at 28-29°C. n = 5 per group.
F. Tissue weight normalized to body weight of Control and E4BP4-OE mice fed a HFD at 28-29°C. n = 5 per group.
G. Left: representative images of Hematoxylin and eosin (H&E) staining of iBAT from control and E4BP4-OE mice fed a HFD at 28-29°C. Scale bar: 50μm. Right: Lipid droplet area quantification. n = 3 per group.
H. Images of mitochondrial iBAT of Control and E4BP4-OE by TOM20 immunocytochemistry Representative image. Scale bar, 50 μm.

For B-G data are presented as mean±SEM. Two-sided P-values were calculated using an unpaired Student's t-test (B, C, E, F, and G). Two-way ANOVA with Tukey's multiple comparisons test (D). *P < 0.05, **P < 0.01, ***P < 0.001.

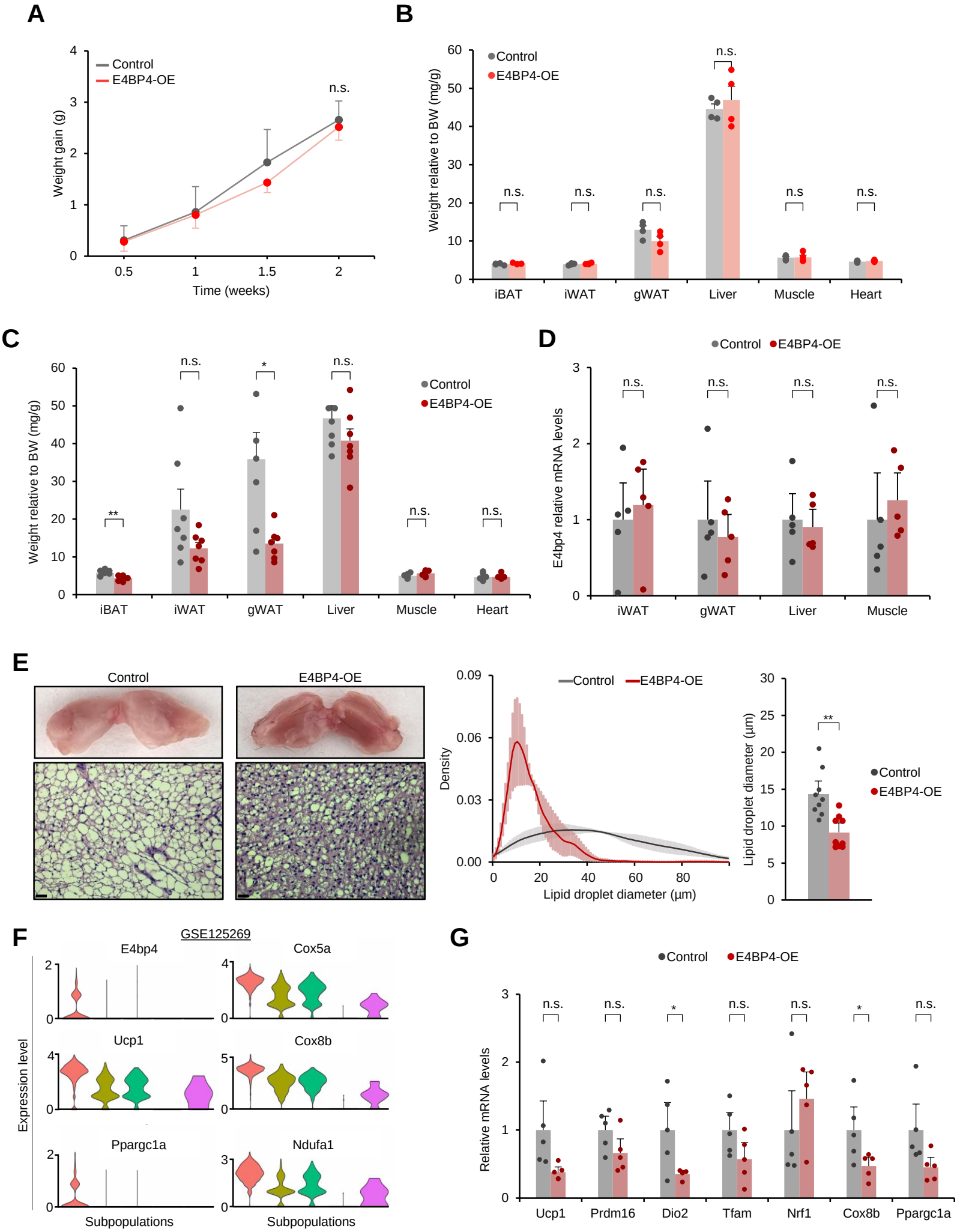
A
Control
E4BP4-OE
Weight gain (g)
Time (weeks)
n.s.
B
Control
E4BP4-OE
Weight relative to BW (mg/g)
n.s.
iBAT
iWAT
gWAT
Liver
Muscle
Heart
C
Control
E4BP4-OE
Weight relative to BW (mg/g)
**
n.s.
*
iBAT
iWAT
gWAT
Liver
Muscle
Heart
D
Control
E4BP4-OE
E4bp4 relative mRNA levels
n.s.
iWAT
gWAT
Liver
Muscle
E
Control
E4BP4-OE
Density
Lipid droplet diameter (µm)
Lipid droplet diameter (µm)
**
F
GSE125269
E4bp4
Cox5a
Ucp1
Cox8b
Ppargc1a
Ndufa1
Expression level
Subpopulations
Subpopulations
G
Control
E4BP4-OE
Relative mRNA levels
n.s.
*
Ucp1
Prdm16
Dio2
Tfam
Nrf1
Cox8b
Ppargc1a

Figure S2. Analysis of E4BP4-OE in DIO mice using AAV adiponectin promoter (Related to Figure 2)

A. Weight of E4BP4-OE or control mice under HFD at 28-29 °C during 2 weeks. n = 4 per group.

B. Tissue weight normalized to body weight of Control and E4BP4-OE mice fed a HFD at 28-29°C during 2 weeks. n = 4 per group.

C. Tissue weight normalized to body weight of Control and E4BP4-OE mice fed a HFD at 28-29°C during 10 weeks. n = 7 per group.

D. Relative mRNA levels of E4pb4 in the indicate tissues of Control and E4BP4-OE mice fed a HFD at 28-29°C during 10 weeks. n = 7 per group.

E. Left: representative images of Hematoxylin and eosin (H&E) staining of iBAT from control and E4BP4-OE mice fed a HFD at 28-29°C during 10 weeks. Scale bar: 50μm. Right: lipid droplet diameter distribution and quantification. n = 3 per group.

F. Violin plots showing the distribution of normalized expression values of indicated genes across cells of the adipocyte clusters.

G. Relative mRNA levels of indicate genes of Control and E4BP4-OE mice fed a HFD at 28-29°C during 10 weeks. n = 7 per group.

For A-E, and G data are presented as mean±SEM. Two-sided P-values were calculated using an unpaired Student's t-test (A-E, and G). *P < 0.05, **P < 0.01, ***P < 0.001.

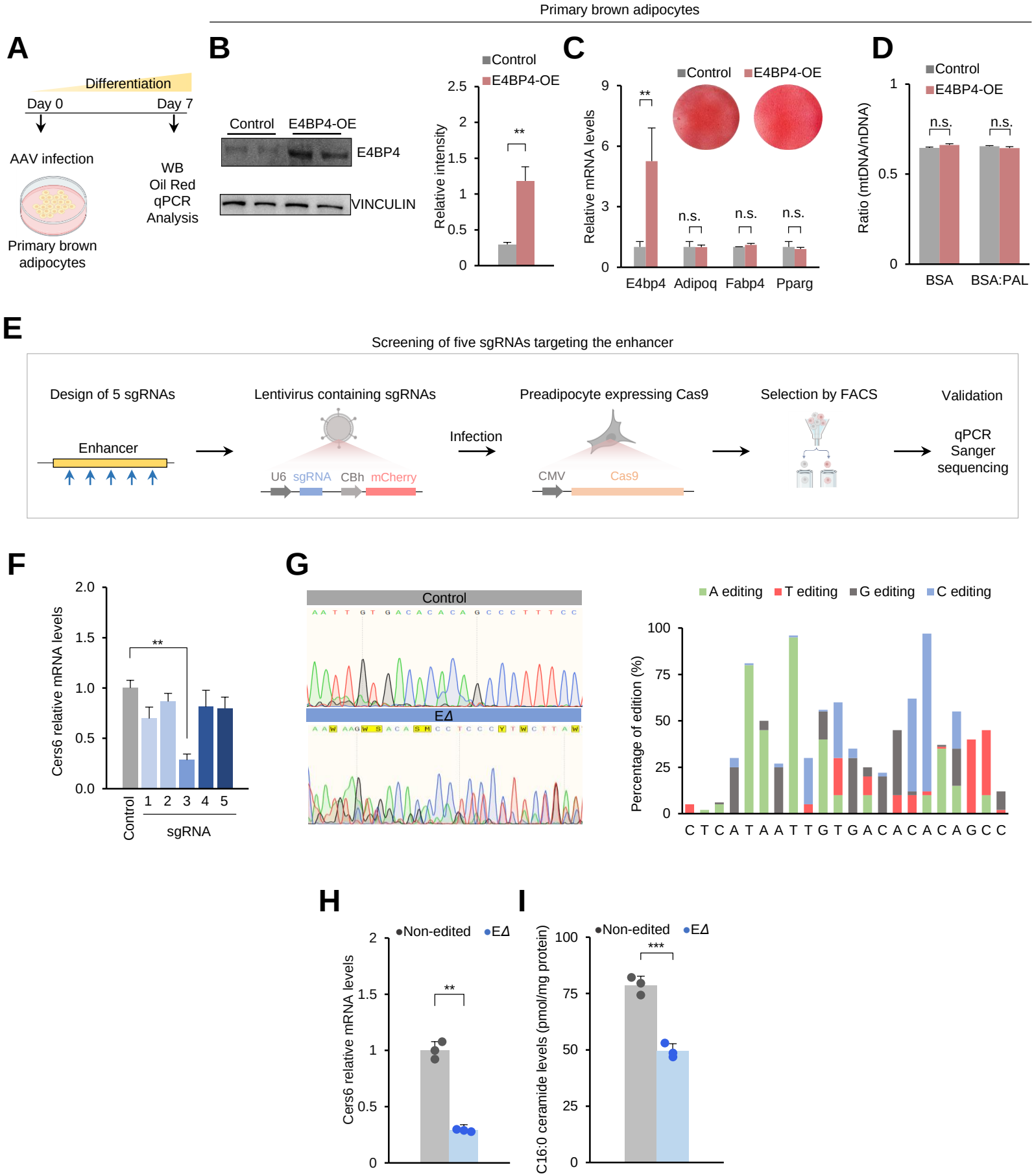
Primary brown adipocytes
A
Differentiation
Day 0
Day 7
AAV infection
Primary brown adipocytes
WB
Oil Red
qPCR
Analysis
B
Control
E4BP4-OE
E4BP4
VINCULIN
Control
E4BP4-OE
Relative intensity
**
C
Control
E4BP4-OE
Relative mRNA levels
**
n.s.
n.s.
n.s.
E4bp4
Adipoq
Fabp4
Pparg
D
Control
E4BP4-OE
Ratio (mtDNA/nDNA)
n.s.
n.s.
BSA
BSA:PAL
E
Screening of five sgRNAs targeting the enhancer
Design of 5 sgRNAs
Enhancer
Lentivirus containing sgRNAs
U6
sgRNA
CBh
mCherry
Infection
Preadipocyte expressing Cas9
CMV
Cas9
Selection by FACS
Validation
qPCR
Sanger
sequencing
F
Cers6 relative mRNA levels
**
Control
1
2
3
4
5
sgRNA
G
Control
EΔ
A editing
T editing
G editing
C editing
Percentage of edition (%)
C T C A T A A T T G T G A C A C A C A G C C
H
Non-edited
EΔ
Cers6 relative mRNA levels
**
I
Non-edited
EΔ
C16:0 ceramide levels (pmol/mg protein)
***

Figure S3. E4bp4 gain-of-function and mutant (ΔE) Cers6 enhancer (E0697815) models in brown adipocytes (Related to Figure 3 and 5)

A. Schematic illustration of experimental design (B-D) for overexpression of E4bp4 (E4BP4-OE) or control in primary brown adipocytes. The cartoon was created using a Biorender.
B. Left: western blotting for E4bp4 in in primary brown adipocytes of Control and E4BP4-OE. Representative results are shown from two independent experiments. Gel source data are presented in the Supplementary data. Right: quantification of western blot.
C. Relative mRNA levels of indicate genes in primary brown adipocytes of the Control and E4BP4-OE groups. n = 3 per group.
D. Ratio of mitochondrial DNA (mtDNA) and nuclear DNA (nDNA) in primary brown adipocytes of the Control and E4BP4-OE groups. n = 3 per group.
E. Schematic illustration of experimental design for the screening of sgRNAs targeting the enhancer (F-G). The cartoon was created using a Biorender.
F. Relative mRNA levels of Cers6 in brown adipocytes mutant E0697815 (ΔE) for the Validation of sgRNA. n = 3 per group.
G. Left: Sequencing analysis of CRISPR/Cas9-mediated enhancer E0697815 (ΔE) ablation in brown adipocytes. Nucleotide sequences of targeted enhancer of cells treated with sgRNA and control. Right: percentage of nucleotide mutations derived from Sanger sequencing data (G).
H. Relative mRNA levels of Cers6 in brown adipocytes mutant E0697815 (ΔE) or Control. n=3 per group.
I. C16:0 quantification by mass spectrometry in brown adipocytes mutant E0697815 (ΔE) or Control. n=3 per group.

For B, C, D, F, H, and I data are presented as mean±SEM. Two-sided P-values were calculated using an unpaired Student's t-test (B, C, D, F, H, and I). *P < 0.05, **P < 0.01, ***P < 0.001.